Faculty of Physics and Astronomy

University of Heidelberg

Master's thesis

in Physics

LEONIE FLOTHOW

born in Tübingen

Bubble characteristics from breaking waves in fresh water and simulated seawater

Referees:
Prof. Dr. BERND JÄHNE
Prof. Dr. NORBERT FRANK

Abstract

The appearance of bubbles was determined in three different wind wave facilities utilizing an optical bright field technique. Based on the bubble detection algorithm by W. Mischler [22], an algorithm has been developed by means of which bubbles and their sizes can be detected automatically. The method is applicable up to moderate to high bubble densities. At the Aeolotron bubble detection up to the water surface is feasible. It has been shown that the density of bubbles correlates to wind speed, water conditions, the distance to the water surface as well as to the tank geometry.
Observations show an increased bubble density in salt water compared to fresh water at the same wind conditions. A study on the influence of lower Butanol concentrations of about $50\,\mathrm{ml\,m^{-3}}$ was carried out. Low Butanol concentrations in the water lead to an increased density of bubbles and additionally, as could be shown in the Aeolotron, a significant increase of very small bubbles ($r < 65\,\mu\mathrm{m}$). Adding Butanol seems to be a good, non-corrosive substitute for sea water. The influence of the fetch length was systematically researched by carrying out measurement series in the annular wind wave facility in Heidelberg as well as measurement series in linear wind wave facilities in Marseille, France and Kyoto Japan, both of which have different sizes and fetch lengths. Comparing these three wind wave facilities a high correlation between the appearance of bubbles and the fetch length could be detected. Analysis of fresh water measurements at hurricane like wind conditions lead to the discovery of a saturation effect on the appearance of bubbles.

Zusammenfassung

In drei verschiedenen Wind-Wellenkanälen wurde das Auftreten von Blasen mithilfe einer optischen Hellfeldmethode untersucht. In Anlehnung an den Blasendetektionsalgorithmus von W. Mischler [22] ist ein Algorithmus entwickelt worden, mit dessen Hilfe Blasen und deren Radien automatisiert detektiert werden können. Diese Methode in zuverlässig anwendbar bis zu mittleren bis hohen Blasendichten und ermöglicht im Heidelberger Wind-Wellenkanal Blasendetektionen bis an die Wasseroberfläche. Die Abhängigkeit der Blasendichten von der Windgeschwindigkeit, den Wasserbedingungen, dem Abstand zur Wasseroberfläche und der Geometrie des Kanals konnte gezeigt werden.
Beobachtungen zeigen ein gesteigertes Aufkommen bei gleichen Windverhältnissen von Blasen in Salzwasser im Vergleich zu Süßwasser. Der Einfluss von geringen Butanolkonzentrationen von etwa $50\,\mathrm{ml\,m^{-3}}$ auf Süßwasser wurde hinsichtlich Blasen untersucht. Genannte Butanolkonzentrationen im Wasser führen zu einer erhöhten Blasendichte und, wie am Aeolotron gezeigt werden konnte, einem signifikaten Anstieg sehr kleiner Blasen ($r < 65\,\mu\mathrm{m}$). Die Zugabe von Butanol scheint ein guter, nicht korrosiver Ersatz für Meerwasser zu sein.
Durch den ringförmigen Kanal in Heidelberg und zwei lineare Kanäle unterschiedlicher Größe und Windstreichlänge in Marseille, Frankreich und Kyoto, Japan, konnte der Einfluss der Windstreichlänge untersucht werden. Im Vergleich der drei Wind-Wellenkanälen zeichnet sich eine starke Abhängigkeit im Blasenaufkommen von der Windstreichlänge ab. Bei Analysen von Süßwassermessungen bei hurrikanähnlichen Windbedingungen (maximales u_{10}=$67\,\mathrm{m\,s^{-1}}$), wurde ein Sättigungseffekt für das Aufkommen von Blasen entdeckt.

Contents

Introduction

Gas exchange takes place at the interface between air and water. These processes are most influencing for human life at the oceans, as water compartment and the atmosphere, as air compartment. Research is conducted to develop models describing gas exchange processes. Several parametrizations try to describe gas exchange in terms of the velocity in ten meter above sea level u_{10} [12], [24].
Beneath exchange at the water surface, breaking waves entrain bubbles into the water bulk. The role of air bubbles is not yet fully understood, but they might contribute in a significant way to transfer processes. Their contribution is influenced by several mechanisms.
Bubbles enlarge the interface due to their additional surface under water. Buoyant degassing enhances turbulence which itself enhances gas transfer. The hydrostatic pressure under water and surface tension both augment partial pressure of individual tracers and thus may lead to supersaturation and even to a complete dissolution of bubbles. This asymmetric effect enhances the invasion of gas due to increased pressure.
To quantitatively analyse the bubble effect, size distributions and some characteristic time scales have to be known. The *residence time* is limited by the rise velocity due to buoyancy. Two *dissolution times* of bubbles are defined as a consequence of increased pressure, the hydrostatic pressure and the surface tension. The *equilibrium time* describes the time until the air in the bubble and the surrounding water are in equilibrium. All these time scales are dependent on the size of a bubble.
Especially the equilibrium time depends on the solubility of a tracer. Those with higher solubility equilibrate faster and, in a first approximation, it can be assumed that the whole bubble volume reaches equilibrium. Low soluble gases take longer to reach equilibrium. Bubbles might even be dissolved, or breach the water surface before equilibrium.
For a better understanding of the role of bubbles in gas exchange and to identify regimes of importance for low and high soluble gases, replicable measurements are needed. Those can give insights in the transport mechanisms, also via air bubbles. Experiments in laboratory facilities are very promising to reproduce same conditions. Laboratory experiments facilitate the variation of only some specific parameters. On the same time a bunch of environmental parameters is measurable. The downside of most wind wave channels is the water quality. Most of the facilities are not suitable for seawater, which is very corrosive due to its salt content. The difference between salt water and fresh water is considerable, in particular for bubble formation processes. At first sight, seawater tends to form more, especially small bubbles.

Goal of this work

For laboratory experiments a substitute for seawater is of great interest. An alternative which does not contain corrosive salt and which is easy to prepare would significantly im-

prove laboratory experiments. It is observable that a low Butanol concentration in water changes the occurrence of bubbles. In general more bubbles and smaller bubbles are apparent. Whether Butanol is a good alternative and how it changes the bubble formation and occurrence should be shown in this thesis. The comparison with proper seawater is a subsequent aim.
Furthermore, the role of bubbles for gas exchange should be investigated by bubble observations. Previous experiments show an additional increase in gas exchange from wind speeds of about $u_{10} = 35\,\mathrm{m\,s^{-1}}$ on, Krall [19]. This increase is likely to be in parts of bubble origin. Bubble measurements over a wide range of wind and water conditions will reveal new information about bubble occurrence. The aim is to characterize the change in bubble spectra which is supposed to happen at around $u_{10} = 35\,\mathrm{m\,s^{-1}}$.
To accomplish the stated objectives, bubble measurements are performed at three laboratory facilities of different geometry and size.

1. Theoretical background

1.1. Gas exchange

The transport of gas or more general a tracer between liquid and gaseous media is driven by molecular and turbulent diffusion. Molecular Diffusion is a result of random thermal motion. A concentration difference results in an effective tracer transport.

In the case of a vertical concentration gradient, molecular diffusion leads to a net flux from higher to lower concentrations described by Fick's 1st law in (1.1).

$$j = -D \cdot \frac{\partial c}{\partial z} \tag{1.1}$$

j being the net flux, D the molecular diffusion coefficient and c the concentration of a tracer.

Equation (1.1) can be extended by the turbulent diffusion coefficient $K_c(z)$ that is dependent on the distance to the boundary layer. The resulting flux density is described by eq. (1.2) [15].

$$j = (D + K(z))\frac{\partial c}{\partial z} \tag{1.2}$$

The variable that describes the amount of a tracer passing through the surface per time is in the unit of a velocity $\mathrm{m\,s^{-1}}$ and is called transfer velocity. Equation (1.3) defines the transfer velocity k as the flux density per concentration difference.

$$k = \frac{j}{c_{\mathrm{surf}} - c_{\mathrm{bulk}}} \tag{1.3}$$

c_{surf} is the concentration at the surface and c_{bulk} the concentration in the bulk at a reference level. Both, at the air-side and at the water-side, a mass boundary layer exists. The one with the larger transfer resistance or smaller transfer velocity dominates the transfer process. At the interface a thermodynamic solubility equilibrium is assumed thus the tracer's concentration is discontinuous at the surface due to Henry's law eq. (1.4), which reads:

$$c_{\mathrm{water}} = \alpha \cdot c_{\mathrm{air}} \tag{1.4}$$

Where α is the tracer dependent dimensionless solubility. A higher solubility leads to an air-side mass boundary layer control and vice versa, see Jähne [15]. Beneath these general transfer mechanisms at an interface, bubbles entrained by breaking waves contribute to the transfer in a specific way.

1.1.1. Influence of bubbles

Bubbles might have a significant influence on the transfer velocities depending on the wind and water conditions and the tracer specific solubility.
Bubbles affect the transfer velocity by different mechanisms:

- Bubbles provide an additional surface where exchange of a tracer can take place. The contribution of a bubble of radius r is proportional to the concentration difference $(c_w - c_b)$ and described by a net flux J:

  $$J = 4\pi r^2 \cdot j \cdot (c_w - c_b)$$

  where j is the 'individual bubble transfer velocity' (Jähne [17] and Woolf [31]), c_w concentration in the water and c_b concentration at the interface. With $c_b = \alpha \cdot p_b$ and p_b being the partial pressure of the gas in the bubble.

- Henry's law states that the equilibrium concentration is proportional to the partial pressure in the gas phase. A high hydrostatic pressure as well as additional surface tension might lead to supersaturation and such enhance the gas exchange.

- Bubbles created by breaking waves enhance the near surface turbulence resulting in an increase in gas transfer [15].

Gases with high solubility quickly come into equilibrium for gas transport from the atmosphere to the ocean. For those gases bubbles contribute to the exchange only for a very short time and the effect on the exchange rate is rather small. Bubbles have a larger relative impact for gases with lower solubility since they contribute for a larger fraction of their lifetime.
Net air-sea flux of a gas can be described by eq. (1.5) where k_b is the contribution of bubbles to the air-sea transfer rate [30].

$$F = (k_0 + k_b)[c - \alpha \cdot p(1 + \Delta)] \tag{1.5}$$

The partial pressure of the gas in the lower atmosphere is named p, α is the solubility of the gas and Δ is a value which estimates the equilibrium supersaturation.

1.2. Bubble visualisation method

There are many ways to measure bubble distributions. In addition to the here mentioned optical methods, acoustical methods are widely used as for instance in Breitz [4], Deane [8], Medwin [21], and Su [28].

1.2.1. Bright field method

To image air bubbles under water a bright field method can be used. The light source is opposing the camera. Without bubbles the sensor is evenly illuminated. Bubbles entrained into the water due to breaking waves refract the light with the result that no light reaches the camera sensor through the bubble. Depending on the incident angle or distance to the central ray respectively a shadow of the bubble is imaged to the camera as shown in fig. 1.1, from [10]. An exception is the central ray penetrating the bubble perpendicular to the surface which goes straight through the bubble and can be imaged for large bubbles.

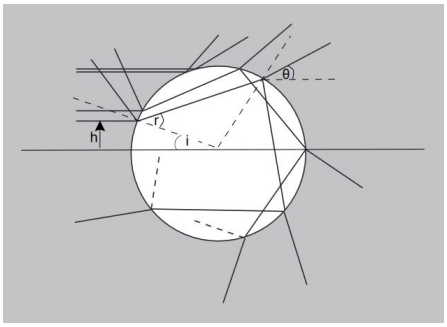

Figure 1.1.: Bright field method

1.2.2. Dark field method

Dark field methods illuminate passively from the side or from the back with divergent rays. In the absence of bubbles no light is directed to the cameras sensor. Light gets refracted at the bubbles surface and thus partly redirected to the sensor. An example for a dark field image is shown in fig. 1.2b.
Detailed description of different visualisation techniques can be found in Balschbach [1].

The three measurement campaigns, investigated for this thesis, all use a bright field technique to visualize bubbles.

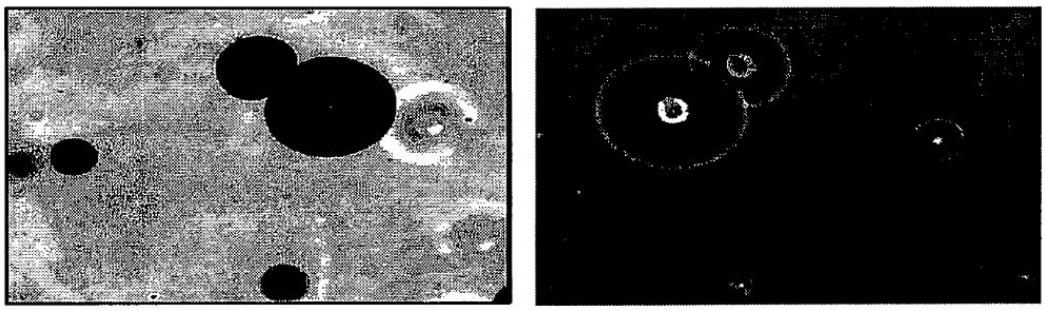

(a) (b)

Figure 1.2.: Images obtained by a bright field method (a) and a dark field method (b), taken from [1].

1.3. Basics in image processing

In this section some basics in image processing, which are used in the detection algorithm and for data evaluation are explained. For further reading, we recommend Jähne [16].

1.3.1. Convolution

The discrete convolution is one of the most important tools in image processing. The convolution with a filter mask can be seen as a weighted averaging where the filter mask determines how the original picture is modified. It can be used for smoothing, to build the derivative and other linear operations [16] . The continuous description of a N-dimensional convolution reads as follows:

$$g(x) * h(x) = \int_{-\infty}^{\infty} h(x') \cdot g(x - x') d^N x' \quad . \tag{1.6}$$

Analog to eq. (1.6) the discrete convolution in one or multi dimensions is constituted by:

$$g'_n = g(x) * h(x) = \sum_{n'=0}^{N-1} h_{n'} g_{n-n'} \tag{1.7}$$

$$g'_{m,n} = \sum_{m'=0}^{M-1} \sum_{n'=0}^{N-1} h_{m'n'} g_{m-m',n-n'} \tag{1.8}$$

At the edge of a picture there are three possibilities to perform the convolution. Either a cyclic extension, a repetition of the edge pixels or all pixels that extend beyond the picture dimensions are set to zero. The latter is used for all convolutions performed in this work. Thereby areas are formed at the edge that can not be used for further evaluation since artificial filtering effects occur. These edges are cut-off, thus neglected.

1.3.2. Gradient

A very useful property of a picture is its gradient. In a continuous description the gradient of a function of two variables is defined as eq. (1.9).

$$\nabla I = \frac{\partial I}{\partial x}\hat{e_x} + \frac{\partial I}{\partial y}\hat{e_y} \tag{1.9}$$

A corresponding discrete filter mask for a central difference is in the form of eq. (1.10) for the horizontal and eq. (1.11) for the vertical direction.

$$d_x = [-101] \tag{1.10}$$

$$d_y = \begin{bmatrix} -1 \\ 0 \\ 1 \end{bmatrix} \tag{1.11}$$

The horizontal and vertical gradients $d_x I$ and $d_y I$ are obtained by convolution with the intensity picture $I(x, y)$.

$$d_x I = d_x * I(x, y) \qquad , \qquad d_y I = d_y * I(x, y) \tag{1.12}$$

The absolute value of the gradient is an important feature, especially for the bubble detection algorithm. The gradient is a measure of depth from focus. It can be calculated from the discrete derivatives $d_x I$ and $d_y I$.

$$|\nabla I| = \sqrt{(d_x I)^2 + (d_y I)^2} \tag{1.13}$$

1.3.3. Dilation and maximum filter

A maximum filter is a non-linear neighbourhood operator and a typical rank value filter. It sorts all grey values within the filter mask and writes the maximum value to the respective pixel. Median and minimum filter work the same way only with another selection criterion for the chosen value. The size and shape of the filter determines the effect on the structures of the picture and is often called structuring element. Gray-scale dilation using a flat structuring element is equivalent to a maximum filter operation. A general form of gray-scale dilation of A by B can be written as eq. (1.14) where D_B is the domain of the structuring element B.

$$A \oplus B(x, y) = max\{A(x - x', y - y') + B(x', y') | (x', y') \in D_B\} \tag{1.14}$$

In this thesis dilation is mainly used to obtain a background picture by eliminating objects. This is relevant for the Aeolotron data evaluation where the background is rapidly changing due to the slightly moving mirror which is used to redirect the background light.

1.3.4. Smoothing

Smoothing of a picture is done by onedimensional binomial filters $b_{x/y}$ shown in eq. (1.15) and eq. (1.16). For symmetry reason an odd number of coefficients is necessary. The horizontal and vertical filter can be applied successively.

$$b_x = \frac{1}{4} \cdot [121] \tag{1.15}$$

$$b_y = \frac{1}{4} \cdot \begin{bmatrix} 1 \\ 2 \\ 1 \end{bmatrix} \tag{1.16}$$

1.3.5. Discrete Fourier transform

The Fourier transform is a useful tool for spectral analysis. It transforms space- or time-based data into frequency-based data. The continuous Fourier transform is given by eq. (1.17).

$$\tilde{g}(k) = \int_{-\infty}^{\infty} g(x)\ e^{-2\pi i k x} dx \tag{1.17}$$

The discrete Fourier transform of a vector g_n of length N is a vector $\tilde{g}_{\tilde{n}}$ of the same length, see eq. (1.18).

$$\tilde{g}_{\tilde{n}} = \frac{1}{N} \sum_{n=0}^{N-1} g_n\ e^{-\frac{2\pi i n \tilde{n}}{N}} \quad , \quad \tilde{n}\ \in\ [0, N-1] \tag{1.18}$$

Usually the discrete Fourier transform (DFT) is performed by a fast Fourier transform algorithm. This reduces the computational complexity for a one-dimensional transformation from $O(N^2)$ to $O(N \cdot log(N))$. DFT is used in this thesis to realize a low-pass filter for the detection of overlapping bubbles, details in sec. 2.3.2.

2. Image processing

In this chapter, the bubble detection algorithm is treated. Therefore some imaging properties of bubbles, that are used in the algorithm, must be stated. Various backgrounds are present due to the different experimental set-ups. In sec. 2.2 preprocessing steps, such as the normalization and a drift correction, are presented. Finally, in sec. 2.3, the developed algorithm and complementary functions are examined.

2.1. Imaging properties of bubbles

For bubble detecting algorithms some imaging properties of bubbles have to be discussed. Especially the gradient at a bubble's edge plays an important role for detection and depth determination.

The connection between a point in the object plane and the image plane is described by the point spread function (PSF) $g(x)$. Mathematically the image $h(x)$ at the image plane can be expressed by the convolution of the object function $f(x)$ with the PSF $g(x)$.

$$h(x) = \int f(x') \cdot g(x - x')dx' \qquad (2.1)$$

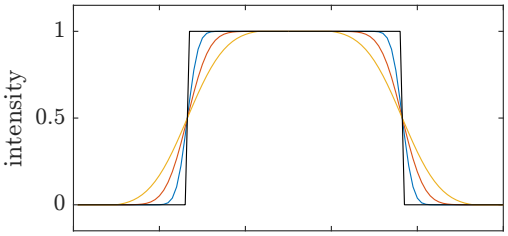

Figure 2.1.: Step function Θ in black (two-sided). Convolution of Θ with Gaussian functions $g(x)$ with different σ in blue, red and yellow.

The PSF consists of a depth dependent blurring part and a diffraction part which is constant for a fix optical system. In the focal plane the PSF consists only of the diffraction part, which occurs due to diffraction at the aperture and can be described by a Gaussian function. A one dimensional description of the system is reasonable justified as long as the object is much larger than σ of the Gaussian function. Within the one dimensional description the edge of the bubble is described by the step function $\theta(x)$.

$$\begin{aligned} \Theta &= 0 && | \text{ if x} < 0 \\ \Theta &= \frac{1}{2} && | \text{ if x} = 0 \\ \Theta &= 1 && | \text{ if x} > 0 \end{aligned}$$

The gradient $h'(x)$ of a depicted bubble in the focal plane is then described by the derivative of the convolution of Θ with $g(x)$.

$$\begin{aligned} h'(x) &= \frac{d}{dx}[\Theta(x) * g(x)] \\ &= \frac{d}{dx}\int \Theta(x-x') \cdot g(x')dx' \\ &= \int \delta(x-x') \cdot g(x')dx' \\ &= g(x) \end{aligned} \tag{2.2}$$

Assuming a Gaussian PSF g(x) and the edge to be at $x = 0$, the gradient is maximal at this position and is equal to

$$h'(x=0) = \frac{1}{\sqrt{2\pi\sigma^2}} \qquad \text{with} \quad g(x) = \frac{1}{\sqrt{2\pi\sigma}} e^{-\frac{x-x_0}{2\sigma^2}} \tag{2.3}$$

When the object is not in the focal plane, defocussing of the image is described by a depth dependent PSF. The PSF has the shape of the used aperture and is thus a circle [16]. A depth dependent PSF is determined to quantify the measurements depth of field, see sec. 4.1.1.

The size of bubbles is determined at half of their maximal grey value. Which is correct for bubbles being larger than PSF. Fig 2.1 shows a simulation in one dimension for different PSF (σ). Here, maximal grey values of one are reached. For smaller bubbles the size at half maximum is an approximation which is simple and therefore easy to apply. At least in a certain depth range and for bubbles larger than a critical bubble size, it is reasonable to calculate like this. Further investigation of the quality of size determination is performed in sec. 4.4.

2.2. Preprocessing

Before one can detect bubbles in the measurement pictures, they have to be preprocessed. Background intensities vary over the field of view which can be corrected by normalization. Furthermore a detailed analysis of background anomalies of the different experiments and the resulting drift and scatter corrections is given.

2.2.1. Normalization

Ideally, the background should be homogeneously lighted. Due to the finite extend of the light sources and other constructive constraints this is usually not the case in the experiments. A correction by a background image, also called zero image, taken in calm water is necessary. This correction should lead to a homogeneous background with grey values of one in the measurement picture. Shadows caused by bubbles have intensities around zero in the normalized image. Every experiment has specificities to obtain a meaningful background image such as a changing illumination or particles affecting the background. How the zero images are taken in the individual experiments, is explained in the respective section in chapter 3. Every image sensor has a certain dark signal I_d. It has to be corrected for I_d by subtracting it from the raw image I_raw and the background image I_0. To be able to

apply this simple one dimensional model, images where the object has grey values of one, the background has values of zero and the edge has intensities between zero and one, are needed. Therefore pictures are inverted.

2.2.2. Drift correction

The drift correction is relevant in particular for the measurements in Kyoto, where high bubble densities are obtained. It is observable that bubble clouds reduce the background intensity due to scattering. This results in an evenly darkened background which is problematic for bubble detection. Another reason for a global reduction of background intensity is a fluctuating light source. This phenomenon is not observed explicitly but cannot be ruled out either. It is assessed as a minor factor. Since the absolute gradient is decisive of counting an object or not, a global reduction in background intensity would lead to systematic lower gradients. A factor f_d corrects for the global intensity reduction.

2.2.3. Scatter correction

The scatter correction is relevant in particular for the measurements in Marseille and Heidelberg. It is observed that bubbles and particles do not cause the expected intensity reduction to zero. An attempt at an explanation could be scattering of light from other bubbles. Since the aperture angle is rather small this should not have a large effect. The fluorescent dye Pyranine, which is added for the wave height measurement (see sec. 3.4.1), emits around $\lambda = 512\,\mathrm{nm}$ and is thus detectable by the bubble camera. Pyranine is excited by a laser with a temporal delay to the bubble camera of 300 µs to 1.8 ms, see fig. 3.7 for Luminy and fig. 3.10 for the Aeolotron measurements. Common fluorescence lifetimes are in the order of ns. Thus the effect of the fluorescent light is expected to be rather small.
Still, systematic higher intensities of the bubbles shadow would lead to systematic lower gradient values. It is assumed that this increase in intensity can be seen as a systematic offset and a scatter factor f_s corrects for it.

Kyoto

The corrected, normalized and inverted picture I for the measurements in Kyoto is then defined as written in eq. (2.4).

$$I_1(x,y) = 1 - \frac{I_\mathrm{raw}(x,y)}{I_0(x,y)} \quad , \quad f_\mathrm{d} = \frac{I_{1,min} + I_{1,\mu}}{2} \quad , \quad I = \frac{I_1 - f_\mathrm{d}}{1 - f_\mathrm{d}} \tag{2.4}$$

I_raw is the raw image. I_0 is the mean of 25 background images. These images are taken during calm water conditions. The drift factor f_d is calculated as the arithmetic mean of the minimal grey value $I_{1,min}$ and the centre of gravity $I_{1,\mu}$ of grey values between 0 and 0.8 of I_1. Especially for measurements with Butanol added to the water a drift in the background over time can be observed. An explanation for this drift could be a decrease in concentration of Butanol resulting in lower bubble densities. Fig. 2.2 shows the temporal evolution of the minimal background intensity in the inverted pictures for the highest wind condition with added Butanol. Background intensities should be close to zero, bubbles should have grey

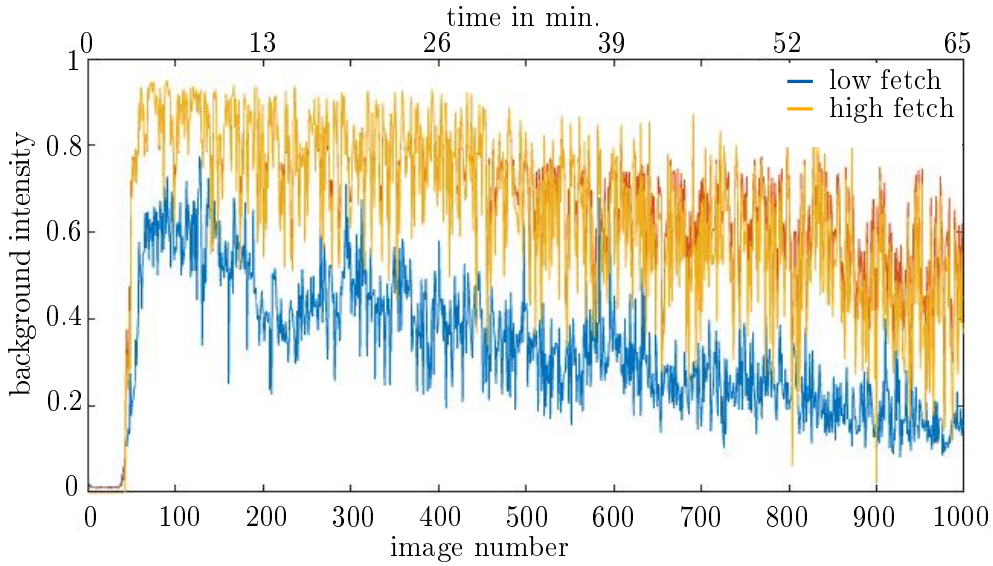

Figure 2.2.: Temporal evolution of the background intensity per picture over 65 min for Butanol conditions at $f_{\mathrm{ref}} = 800\,\mathrm{rpm}$, at the high fetch (yellow) and at the low fetch (blue).

values around one. Due to the drifting background, f_{d} is calculated for every picture. Dark images are negligible due to the very small exposure time of 250 µs.

Aeolotron Heidelberg

A changing background, caused by the mirror redirecting the illumination light, makes the Aeolotron data challenging. The background intensities are changing, since the mirror moves with the wave movement. A separate zero image is needed for each picture. It is obtained by dilation (sec. 1.3.3) of the original bubble picture. A structuring element is chosen so that all objects are filtered out and a reasonable smooth and flat background is obtained. Therefore a ball-shaped non-flat structuring element with $size = 50\,px$ and $norm = 10$ is used. The *size* represents approximately the size of the largest objects. The *norm* is a sort of weighting area. The dark image is negligible due to the camera settings. It is zero for all pixels and thus not relevant.
Zero images obtained by dilation are not value-conserving. Thus the zero image and the bubble image have to be normalized by the maximum grey value of the images.

$$I_{\mathrm{raw,norm}} = \frac{I_{\mathrm{raw}}}{max(I_{\mathrm{raw}})} \quad , \quad I_{0,\mathrm{norm}} = \frac{I_0}{max(I_0)} \tag{2.5}$$

The general way to calculated the corrected, normalized and inverted images I is shown in eq. (2.6).

$$I_1 = \frac{I_{\mathrm{raw,norm}}}{I_{0,\mathrm{norm}}} \quad , \quad I = 1 - \frac{I_1 - f_{\mathrm{s}}}{1 - f_{\mathrm{s}}} \tag{2.6}$$

The correction factor f_{s} accounts for scattering. It is calculated from minimal and maximal

grey values by an adapted way of smoothing and application of minimum and maximum filters. More precisely, the minimum and maximum value of the central part (y=300:699, x=100:499 in px) of every image in the whole time series is identified. Only the central part is taken since intensity fluctuations are less extreme there. Furthermore the minimum should be the result of a bubble or dirt particle. For low bubble concentrations this is ensured by a minimum filter over about 30 images. This leads to a vector $v_{\min}$ containing minimum values of the time series. Since maximum values are less sensitive to distortion a simple smoothing, described in eq. (1.15), is applied resulting in a vector $v_{\max}$ of maximal intensities. No drift in intensities over time is observed, hence f_s is calculated once for each measuring cycle, which lasts five.

$$f_s = median\left(\frac{v_{\min}}{v_{\max}}\right) \tag{2.7}$$

Luminy Marseille

Usually a background image is taken at calm water conditions before or after the measurement. During the Luminy measurements many particles are dispersed in the water, making the background images not representative for the background illumination. For each condition a background image is developed by image processing, using dilation (see sec. 1.3.3) and subsequent averaging of about 200 bubble pictures. Pictures of different times during the measurement are selected. The structuring element for dilation is the same as for the Aeolotron data. The dark image is negligible due to the camera settings. It is zero for each pixel and thus not relevant.
The scattering factor f_s for the Luminy data is determined in the same way as at the Aeolotron, Heidelberg. A measuring cycle at Luminy lasts five or ten minutes.

2.3. Algorithm

In this section the algorithm used for automated bubble detection is described. The algorithm is based on concepts of Mischler [22] and Honkanen [14]. Mischler compares four bubble detecting algorithms. The recommended algorithm uses a segmentation at half maximum of the grey values and analyses overlapping bubbles. These two properties are included for detection. In the following, details about the implemented algorithm and complementary functions are given. Attempts are made to take full advantage of bubble specific properties to not detect any dirt particle. Nevertheless, particles resembling bubbles in their shape may be detected as bubbles. Some examples of detected asymmetric objects are presented in fig. 2.3

2.3.1. Bubble detection

Fig. 2.4 shows details about the bubble detecting algorithm. It is the version as it is used for data recorded in Luminiy and at the Aeolotron. The preprocessing for the data of Kyoto is slightly different, as described in sec. 2.2. Once the corrected and normalized image I is obtained, the following steps are identical. The main compartments of the algorithm are highlighted in different colours. The preprocessing section has a grey background. Identifying and consecutively numbering of objects, also called labeling, is shaded in red. The

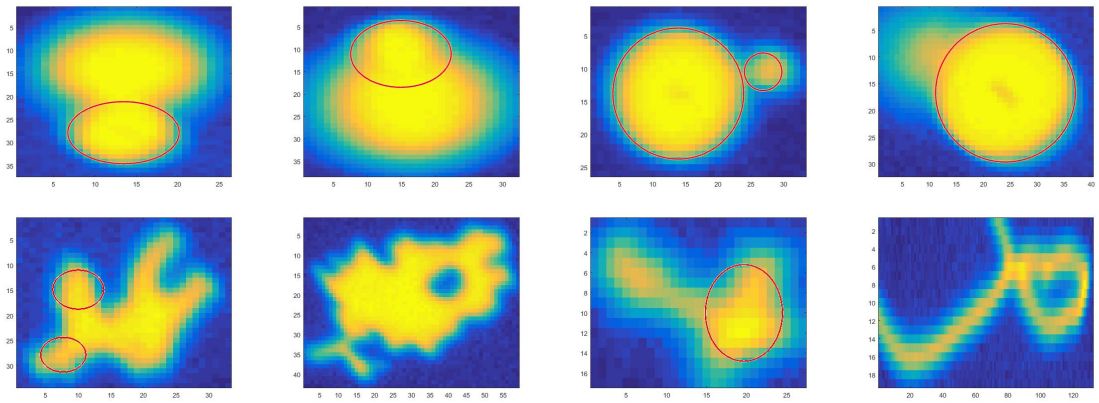

Figure 2.3.: Examples of asymmetric objects. Red circles indicate detected bubbles.

bubble size determination is in shaded in yellow.

Starting with the raw image I_{raw} an exclusion criterion for an image is its maximum and minimum value ('max min'). Images taken above the water surface are widely overexposed or underexposed. This is reflected in the pictures maximum or minimum intensity value. Pictures with intensity values above 250 (of 255) or below 5 are not taken into account. For valid pictures an inverted, normalized and background corrected image I is obtained by dilation, smoothing and normalization to maximum values. From I a binary image I_{bin} is created with a threshold of 0.5. Labeling produces an image I_{label} similar to I_{bin} where every connected area, also referred to as object, is numbered by consecutive numbers. A bounding box describes a rectangular area around the object. Furthermore the length of the major and the minor axis $l_{\text{maj}}, l_{\text{min}}$ of the object is determined by the eigenvalues of the covariance matrix. Every bounding box is successively examined for several criteria. If an image contains an object with $l_{\text{maj}} > 200\,px$, the image is skipped. Such large objects are either enormous conglomerates of bubbles, what makes a good detection very unlikely or the image is taken close to the water surface and where the illumination becomes random. If an object ranges to an edge of the FOV, the object is not considered. Usually this is the case for bubbles partly in the FOV. Especially at high bubble densities neighbouring objects might reach into other bounding boxes. Therefore only the object with the longest contour is taken into account. The contour is obtained by the MATLAB built in function *contourc*, which provides isolines of a given matrix. The height of the isolines can be chosen. For our purpose it is typically defined as $0.5 \cdot l.m.$, with $l.m.$ being the local maximum grey value. Subsequently a criterion for symmetry is tested. If l_{maj} and l_{min} differ more than 3 pixels the object is treated as an asymmetric object. Asymmetric objects are assumed to be overlapping bubbles. The separation of overlapping bubbles is described in sec. 2.3.2. For symmetric objects with $l_{\text{maj}} > 20$px the central beam can lead to a loss in intensity. To avoid wrong detections the central part of the object is manually set to the maximum grey value within the bounding box. The radius of symmetric objects is determined in two ways. One method is to count pixels with intensities larger than half of the maximum grey value of the object. This gives the area A and thereof the radius is calculated by $r = \sqrt{A/\pi}$.

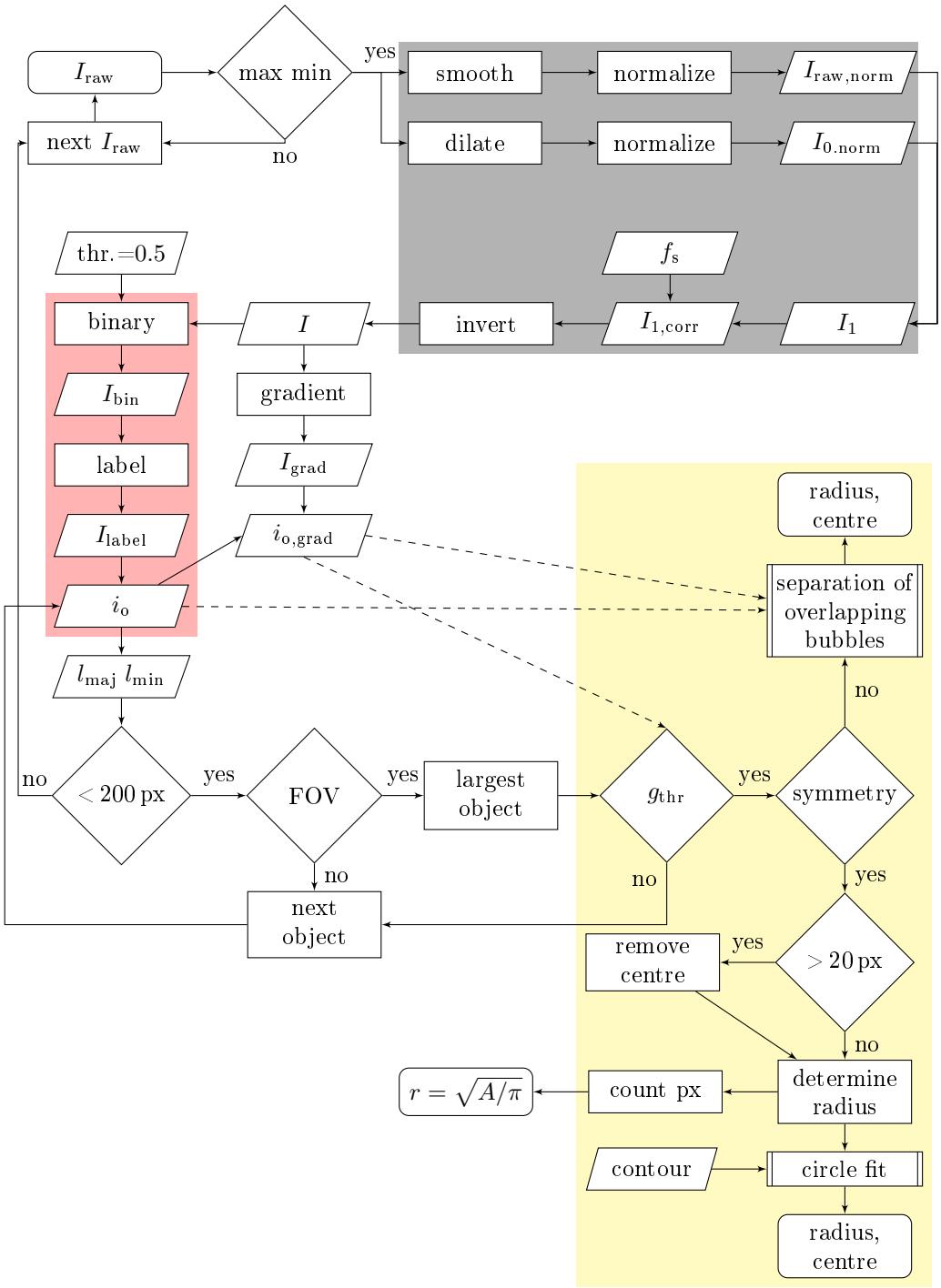

Figure 2.4.: Algorithm for bubble detection and size determination. grey: preprocessing. red: identify objects i_o. yellow: bubble radius determination. Preprocessing slightly varies between the campaigns, see sec. 2.2.

Additionally a circle fit method is used, introduced in sec. 2.3.3. Both fitting methods have difficulties with measuring small bubbles. A comparison is given in sec. 4.4.
Thresholds given in fig. 2.4 are optimized for the measurement campaigns at the Aeolotron.

2.3.2. Separation of overlapping bubbles

The basic idea of how to separate overlapping bubbles is taken from Honkanen [14]. Consider the contour of an object which consists of overlapping bubbles. The contour leads to the curvature, which is positive for a convex shape and negative at a concave shape. At local minima of the curvature, connecting points of bubbles can be assumed. Thus segments of bubbles are received and circles can be fit to the individual segments to obtain their size.

Here a detailed description of the algorithm and more information related to the individual steps is given and depicted in fig. 2.5.
i_o is the part of image I including an asymmetric object. The contour at half maximum height is extracted from i_o. In images of large bubbles, a bright spot appears from the central beam passing the bubble without refraction. In this bright central part a second contour at half maximum intensity is often present. So that N=2, with N being the number of contours. This contour disturbs a correct detection and is thus eliminated artificially. If thereafter another contour is present ($N > 1$) the object gets rejected. A rough estimation of perimeter P and area A covered by the object is done, which is used later. Only closed contours C can be used in this algorithm. This is verified if the first and last point of C are the same. Short contours, as 30 points, cannot be split into multiple parts. If the length of the whole contour C is shorter than 30 points, the object is ruled out. Contours received from *contourc* usually are very wiggeling. For further processing a smooth contour is necessary. This is realized by a low-pass frequency filter. Which transforms x- and y- data of C by a fast Fourier transform and cuts of wiggles with a higher frequency than f_thr (sec. 1.3.5). The threshold proposed by Honkanen [14], is dependent on the length of the contour l and slightly modified to:

$$f_\mathrm{thr} = 0.07 \cdot l \cdot \frac{10}{\sqrt{l+30}} \quad ,$$

which leads to smooth contours C_s without high frequency wiggles. From C_s the curvature κ is determined in multiple steps as follows. The derivative of the x- and y-components of the smoothed contour $C_\mathrm{s,x}$, $C_\mathrm{s,y}$ is calculated by a difference scheme of the general form:

$$f'(t) = \frac{f(t+2) - f(t-2) + 8 \cdot (f(t+1) - f(t-1))}{12} \qquad t \in [1, l].$$

A periodic extension of $f(t)$ has to be performed to calculate $f'(t)$. The slope φ of the perimeter is defined by $\varphi = \arctan \frac{C_\mathrm{s,y}}{C_\mathrm{s,x}}$. Discontinuities arise since the arctangent function returns angles in the range $[-\pi, \pi]$. These discontinuities can be corrected by unwrapping the slope, therefore multiples of 2π are added when absolute jumps between two consecutive elements are greater than π.
φ' is the derivative of φ and calculated by the above mentioned difference scheme. The

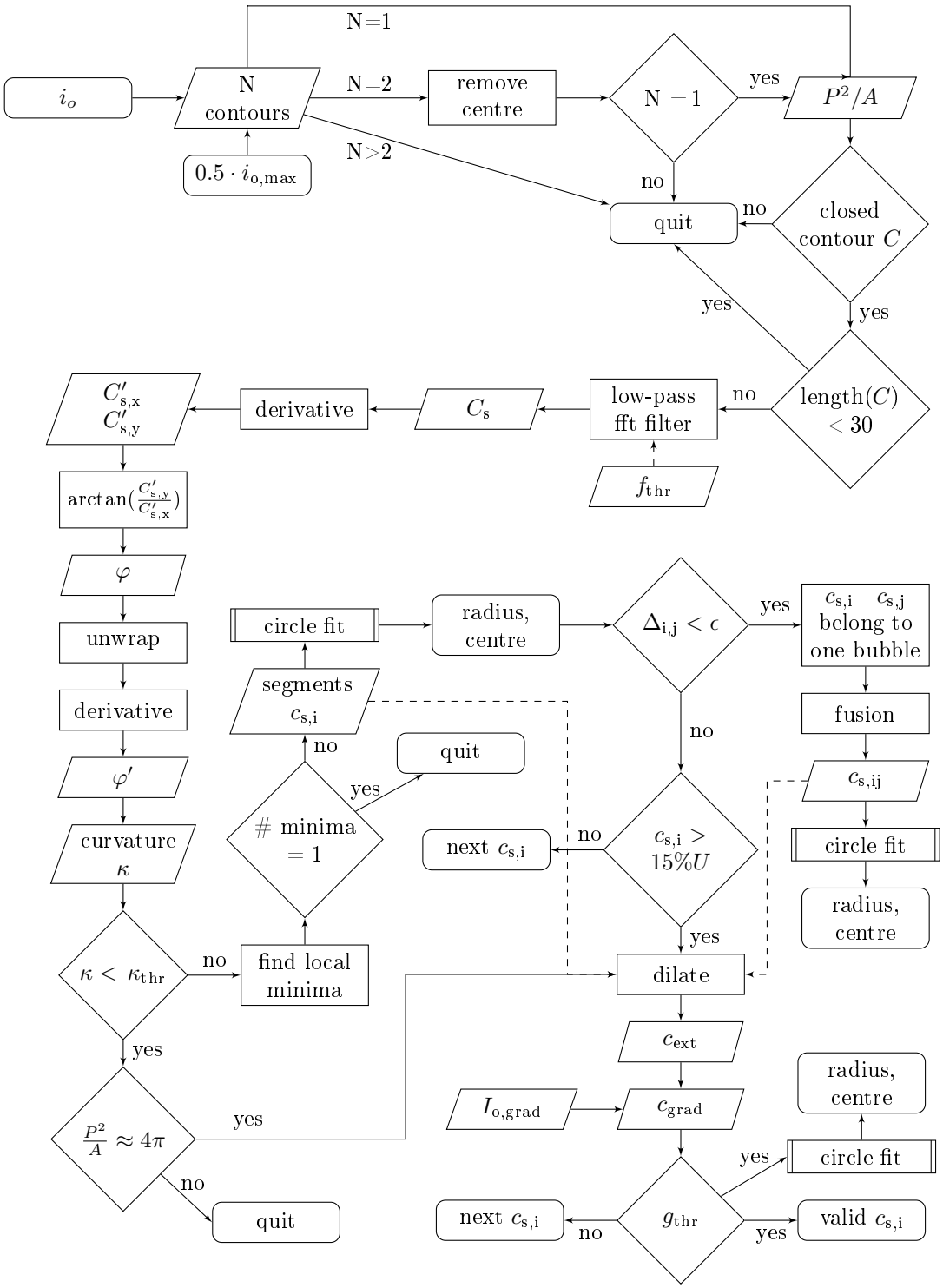

Figure 2.5.: Algorithm for separattion of overlapping bubbles. Details and explanation on variables are given in sec. 2.3.2. Dashed lines indicate an input for an operation.

curvature κ of the perimeter is calculated as

$$\kappa = \frac{\varphi'}{\sqrt{{C'_{\mathrm{s,x}}}^2 + {C'_{\mathrm{s,y}}}^2}} \quad .$$

A positive curvature means that the perimeter is convexe and turns towards the centre. The curvature has a negative sign for a concave slope, which is the case at connecting points of overlapping bubbles. If the curvature has values below the threshold $\kappa_{\mathrm{thr}} = 0.0$, it is searched for local minima. These minima in curvature are taken as the connecting points between objects. If only one local minimum is found it is most likely that no bubble is imaged, rather a dirt particle. Otherwise the contour is split at the connecting points into segments c_{i}, representing the contour segment of bubble i. The function $circlefit$ determines radius and centre of c_{i} as described in sec. 2.3.3. The absolute distance between the centres of two bubbles i and j is indicated as $\Delta_{\mathrm{i,j}}$. If the distance is smaller than $\epsilon = 10$, it is most likely that the segments c_{i} and c_{j} belong to the same bubble. The segments are fused and again, a circle is fit to the fused segment. The used circle fit method is only robust if the length of the segment is larger than $< 15\%$ of the perimeter, which is estimated by $P = 2\pi r$. Finally the gradient of the bubble image at the segment has to be encountered. Therefore a binary image is created with c_{i}. The first and last 10% of c_{i} are neglected since these parts are in the transition area between bubbles and thus not representative for gradients of only bubble i. An extended image c_{ext} of the contour segment is obtained by dilation, with a disk-shaped structuring element of radius 4. Multiplication of c_{ext} with the gradient image of the whole object $i_{\mathrm{o,grad}}$ leads to an image, which includs only gradients of segment i. If the gradient threshold g_{thr}, specific for every experiment, is reached, bubble i is counted with the above calculated radius.

One step back: If no local minima of κ below 0.0 is found, it is possible that one large bubble is imaged and considered as asymmetric due to motion blur. If the ratio of the perimeter squared to the area is approximately $4\pi \pm 0.7$, it is assumed to be a large bubble. The following handling of the gradient is the same as for segments. Finally the radius is determined by the function 'circle fit' .

2.3.3. Circle fit

A fast and simple circle fitting method is explained, taken from Gander [9] and already used in Mischler [22]. This method minimizes the algebraic distance of given points in the plane. The general form of the equation of a circle and some transformation is given in eq. (2.8), with x_0, y_0 being the coordinates of the centre.

$$\begin{aligned} (x_i - x_0)^2 + (y_i - y_0)^2 &= r_0^2 \\ \text{or:} \qquad x_i \cdot 2x_0 + y_i \cdot 2y_0 + r_0^2 - (x_0^2 + y_0^2) &= x_i^2 + y_i^2 \end{aligned} \tag{2.8}$$

This can be written in a matrix representation, see eq. (2.9). $\vec{e_{\mathrm{m}}}$ is a unit vector of dimension m. With known contour points $(\vec{x}, \vec{y})$, the matrix A and vector $\vec{c}$ are given. $\vec{b}$ can be extracted

by right-matrix division.

$$A \cdot \vec{b} = \vec{c}$$

$$\text{with:} \qquad A = (\vec{x}, \vec{y}, \vec{e_{\mathrm{m}}}) \quad , \quad \vec{b} = \begin{bmatrix} 2x_0 \\ 2y_0 \\ r_0^2 - (x_0^2 + y_0^2) \end{bmatrix} \quad , \quad \vec{c} = \begin{bmatrix} x_1^2 + y_1^2 \\ \vdots \\ x_{\mathrm{m}}^2 + y_{\mathrm{m}}^2 \end{bmatrix} \tag{2.9}$$

Centre points (x_0, y_0) and radius r_0 can be calculated from $\vec{b}$, see (2.10).

$$x_0 = \frac{b_1}{2} \quad , \quad y_0 = \frac{b_2}{2} \quad , \quad r_0 = \sqrt{b_3 + x_0^2 + y_0^2} \tag{2.10}$$

This fitting method is robust as long as the given points of the contour cover more than 15% of the expected perimeter, Mischler [22].

3. Experiments

Images recorded in three laboratory facilities are evaluated in this thesis. A brief description of the wind-wave channels at Kyoto University, at IRPHE-IOA in Marseille and the Aeolotron at Heidelberg University and their characteristics is given in this chapter. Information about the measured wind and water conditions is supplied. The various measurement set-ups are described in the respective sections as well as the way how zero and dark pictures are recorded and applied. Several measurement techniques are conducted during the measurement campaigns. Those, directly affecting the bubble measurements, are briefly described and referenced in sec. 3.4.

3.1. Kyoto 2015

Experiments in Kyoto are conducted at a linear high speed wind-wave channel which can be operated at hurricane wind speeds. It has a total length of 15.7 m, a flume width of 0.8 m and a height of 1.6 m. As it is built out of glass, the channel is suitable for optical measurements. The water height is about 0.8 m and the total surface length 12.1 m. At 6.5 m fetch wind speeds up to $u_{10} = 67.1\,\mathrm{m\,s^{-1}}$ can be reached. This very strong wind conditions lead to an enormous entrainment of bubbles and high spray production. As reference for wind conditions usually the frequency f_{ref} of the wind generator is given in rotations per minute (rpm). The Kyoto wind-wave channel operates with tap water, also referred to as fresh water in this thesis. Further details about the Kyoto wind-wave channel can be found in [18]. Measurements are performed by W. Mischler and A. Klein in October/November 2015.

In the following sections, details about the bubble measurement in Kyoto are summarized. First a description of the measurement set-up is given including information about the used cameras and lenses. Challenges of colour images are mentioned. Furthermore, measured water and wind conditions are listed and measurement specific calibration features are described.

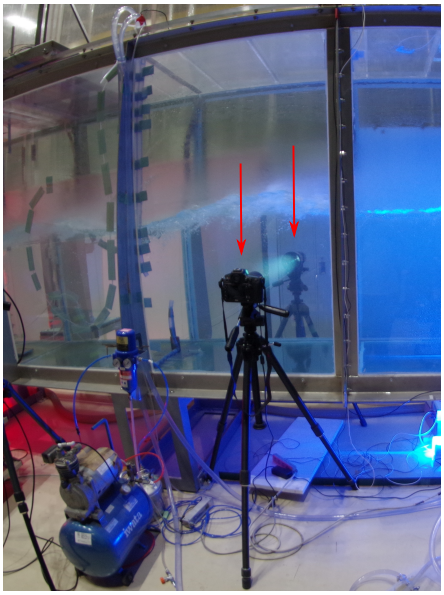

Figure 3.1.: Measurement set-up in Kyoto. The water channel is between camera and light source, both marked with red arrows.

3.1.1. Bubble measurement set-up

Bubble measurements are performed at two different fetches. The measurement section 'low fetch' is situated at 3 m, the section of 'high fetch' at 8 m. A sketch of the measurement set-up is shown in fig. 3.2 and the respective camera and lens settings are listed in tab. 3.1. The illumination and camera systems are set up outside the tank, opposite to each other. Since light is shining through the full 0.8 m width of the channel an intense reduction in background illumination is observed for high wind conditions, due to the amount of bubbles and spray.

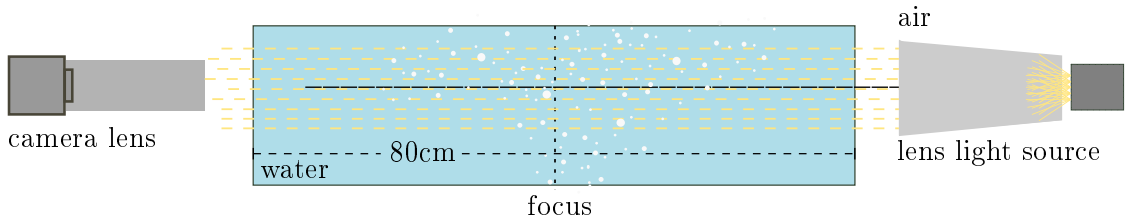

Figure 3.2.: Bubble measurement set-up in Kyoto

Table 3.1.: Camera and lens specifications of the bubble measurement set-up in Kyoto.

Nikon D800 SLR camera	
sensor type	CMOS
sensor size	35.9 mm x 24 mm, 7360px x 4912px
pixel size	4.8 µm x 4.8 µm
lens system camera	f=200 mm, β=1:1, n_f=5.3
lens system light source	f=3 m, n_f=2.8

Colour sensor - Bayer pattern

Images are taken with two Nikon D800 single-lens reflex digital cameras (DSLR). This kind of camera is colour sensitive since a Bayer filter is placed in front of the sensor. A Bayer filter covers 50% of pixels with a green, 25% with a blue and 25% with a red filter. These filters enable to obtain a colour image. Prerequisite for colour images is a polychromatic illumination. The light source consists of blue, green and red LEDs which emit around 470 nm, 530 nm and 670 nm respectively.
For bubble detection only light intensities are relevant. As can be seen in fig. 3.3a the spectral sensitivity of green, red and blue pixels diverges [13]. As a consequence, the absolute intensities of the respective colour pixels diverge. Colour images constitute a second problem: Fig. 3.4a depicts a line profile of the used grating. Maxima and minima correspond to the translucid and optically opaque parts of the grating. Maxima and minima of red, green and blue light are at the same position for the central part of the picture. Fig. 3.4b shows the

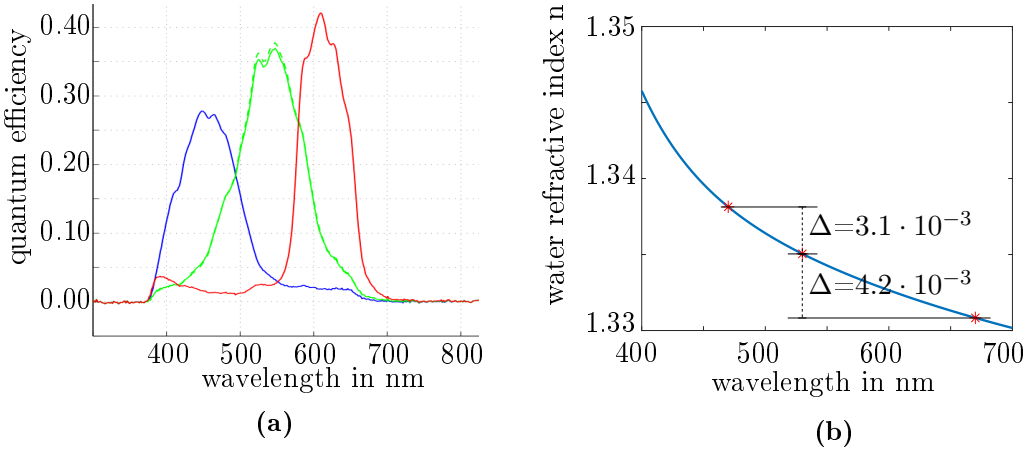

Figure 3.3.: (a) Example for the spectral sensitivity of a CMOS sensor with Bayer filter for blue, green and red light, respectively. (b) Wavelength dependence of the refractive index of water. Wavelengths of blue, red and green LEDs used as light source for bubble measurements are marked as well as the difference in refractive index.

left part of the same line profile. Maxima and minima of red are shifted with respect to the green and blue minima and maxima. An explanation is a lateral chromatic aberration, since the water bulk acts as an optical element. The difference in $n_{\text{water}}(\lambda)$ between green and blue is less due to the closer wavelength peak, see fig. 3.3b. Nervertheless it is unclear, why blue and green seems to be barely shifted.
Additionally longitudinal chromatic aberration leads to different focal lengths. Assuming a water path of 400 mm, it would result in a difference in focal length of about 3 mm between red and blue light.
As a consequence of these chromatic aberrations, only the green filtered pixels are used and missing pixels are interpolated linearly. Larger distances between the evaluated pixels cause a reduction in resolution and could thus lead to additional aliasing [16].

3.1.2. Calibration measurements

Calibration measurements are performed with a rebuilt set-up in Heidelberg, in February 2016. A water tank with dimensions of 300 mm x 300 mm x 600 mm (height x width x depth) is used for the measurements.
All settings are adjusted as good as possible to the settings in Kyoto, still the calibration

Table 3.2.: Camera settings at Kyoto wind-wave channel. Height specifies the distance of the imaging system to the ground of the channel.

frame rate	FOV	t_{exp}	height	β
0.13 Hz	7360 px x 4912 px	250 µs	50 cm	1:0.98

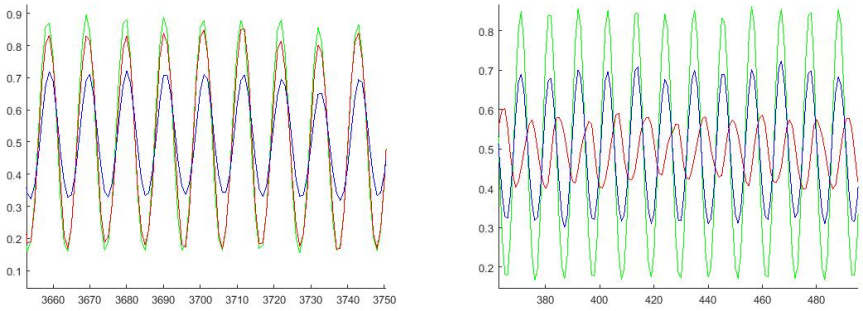

(a) Central part of the gratings profile. **(b)** Left part of the gratings profile.

Figure 3.4.: Line profile of a picture of the used grating. Red, green and blue pixels are interpolated and smoothed separately. Different intensities occur due to different spectral sensitivities. Furthermore the focal length is wavelength dependent and out of focus, extrema are less pronounced. The shift of red towards blue and green extrema is partly explained by the chromatic dependency of $n_{water}(\lambda)$.

should be handled attentively. The measurement set-up at the low and the high fetch are identical in construction. The calibration is only performed for the camera at the low fetch but applied to images of both fetches.
For the determination of the magnification factor β a grating with 500 l.p.i. (lines per inch) is used as calibration target in the object plane. The grating is an optical target which is characterized by constant intervals of bar and space, high edge definition and a high contrast ratio. Distances in the sensor plane are known from pixel dimensions. Thereof β can be calculated, see tab. 3.2. For depth calibration, pictures of the same grating are taken in 10 µm steps covering a depth interval of 2.65 mm. Some depth positions are measured twice.

3.1.3. Measurement conditions

The measurement conditions of the measurement campaign in Kyoto are listed in tab. 3.3. A wide range of wind conditions is covered in Kyoto. Especially the very high, hurricane like wind speeds offer impressive conditions. Those conditions lead to a water loss at the end of the tank due to spray and water patches torn apart from the water surface. To compansate for the loss, fresh water is pumped into the channel at the water entrance.

Butanol

The Kyoto wind-wave channel enables to measure at two water conditions. First, fresh water experiments are conducted. Later, Butanol is added to the water to find out whether low Butanol concentrations in the water volume constitute a non-corrosive seawater model.
The channel has a holding capacity of 13.7 m^3. 700 ml of Butanol is added to the water, which results in an initial Butanol concentrations of $c_0 = 51.1 ml\,m^{-3}$. Due to mass transfer across the interface between water and air a decrease in concentration with time is expected,

Table 3.3.: Wind conditions for fresh water conditions in Kyoto from Takagaki [29]. The supplement '+ Butanol' indicates that measurements are also performed in Butanol conditions. u_{10} and u_* are only available for fresh water conditions and are taken for both water conditions.

water condition	f_{ref} in $m\,s^{-1}$	u_{10} in $m\,s^{-1}$	$u_{*,w}$ in $cm\,s^{-1}$
fresh	200	16.7	0.84
fresh	250	23.75	2.34
fresh	300	29.8	3.10
fresh	350	33.8	5.19
fresh + Butanol	400	40.7	6.13
fresh + Butanol	500	48	7.25
fresh + Butanol	600	56.4	9.37
fresh + Butanol	700	64.3	11.00
fresh + Butanol	800	67.4	11.53

especially for high wind conditions. Additionally, water is blown out of the tank and partly replaced by fresh water. Monitoring of Butanol concentrations is difficult due to an unexpected behaviour of the mass spectrometer. Efforts are made to start experiments with the same initial concentration c_0.

3.2. Luminy - Marseille 2016

In June 2016 experiments are conducted in the Large Air Sea Interaction Simulation Tunnel of the Institut de Rechereche sur les Phénomène Hors Equilibre, Laboratoire Interactions Océan-Atmosphère Luminy (IRPHE-IOA) in Marseille, France. This measurement campaign is called Luminy in the following.

The linear wave channel at Luminy has a length of 40 m, a width of 2.6 m. The water depth is adjustable and at the measurement section usually about 0.9 m. Waves can be produced by wind and by mechanical paddling. Luminy has a recirculating air flow channel with a width of 3.2 m, a height of 1.5 m and a length of 40 m. Reference wind speeds up to $14\,m\,s^{-1}$ are generated by an axial fan located in the recirculation flume. The mechanical paddle can be adjusted by its frequency f_{pad} and amplitude A_{pad}. Measurement instruments are set up at the test section at 28 m fetch, which is equipped with glass windows. Common tap water is used in Marseille and regularly skimming is conducted to reduce surface films. For more information about Luminy see Coantic [6] and Caulliez [5].

In general very little bubble formation can be seen. High numbers of dirt particles are present in the channel despite thorough cleaning. Due to the linearity of the channel, a bottom current opposed to the wind direction is evident and observable.

3.2.1. Bubble measurement set-up

A scheme of the Luminy set-up is shown in fig. 3.5. Camera and lens are built into a waterproof tube. An additional bandpass colour filter for green light ($\lambda = 500\,\text{nm}$ to $550\,\text{nm}$) is attached to the camera to reduce scattering light.

Fig. 3.6 shows a picture of all four measurement systems built up at Luminy. Two of the cameras, named *cam*1 and *cam*4, are installed just below the measurement area of the laser height camera (LHC) [27], in heights $h_1 = 33.4\,\text{cm}$ and $h_4 = 50.5\,\text{cm}$ respectively. The other two cameras, named *cam*2 and *cam*3, are positioned approximately 28 cm upwind of the first measurement section and set up in heights $h_2 = 26.8\,\text{cm}$ and $h_3 = 43.6\,\text{cm}$.

For illumination purpose a light source consisting of 76 green LEDs is used. It is operated with $U = 33\,\text{V}$ and $I_{\text{max}} = 5\,\text{A}$ and has a cylindrical shape with length $l = 15\,\text{cm}$ and radius $r = 13\,\text{cm}$. The LEDs are arranged on one side of the cylinder and a frosted glass screen in front of the LEDs ensures a homogeneous illumination, see fig. 3.6. Due to problems with operating all four light sources simultaneously, the priority is set to *cam*1 and *cam*4 and only the latter two are operated for the whole campaign. As will be shown later, very little bubble formation is observable and only data of the upper camera *cam*4 is evaluated.

Table 3.4.: Camera and lens specifications of the bubble detecting set-up at Luminy.

acA1920 155um – Basler ace	
sensor typ	CMOS – sony IMX174
sensor size	11.3 mm x 7.1 mm, 1920 px x 1200 px
pixel size	5.86 µm x 5.86 µm
lens system	$f = 180\,\text{mm}$, $n_f = 11$

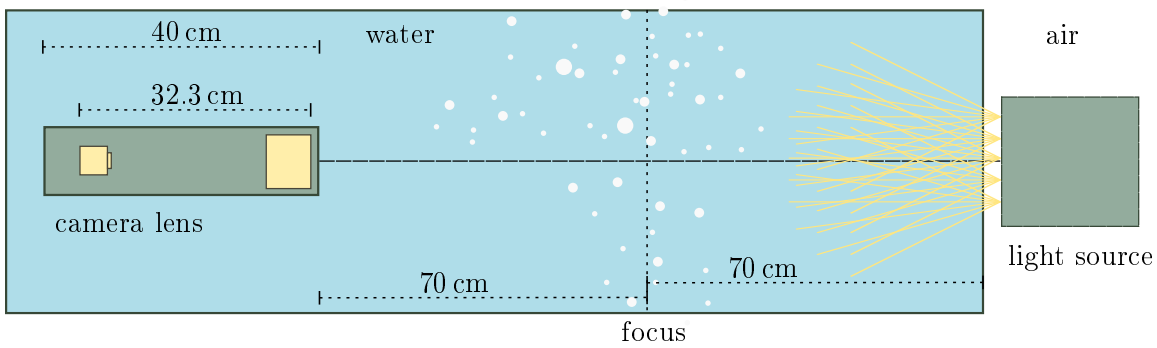

Figure 3.5.: Measurement set-up at Luminy.

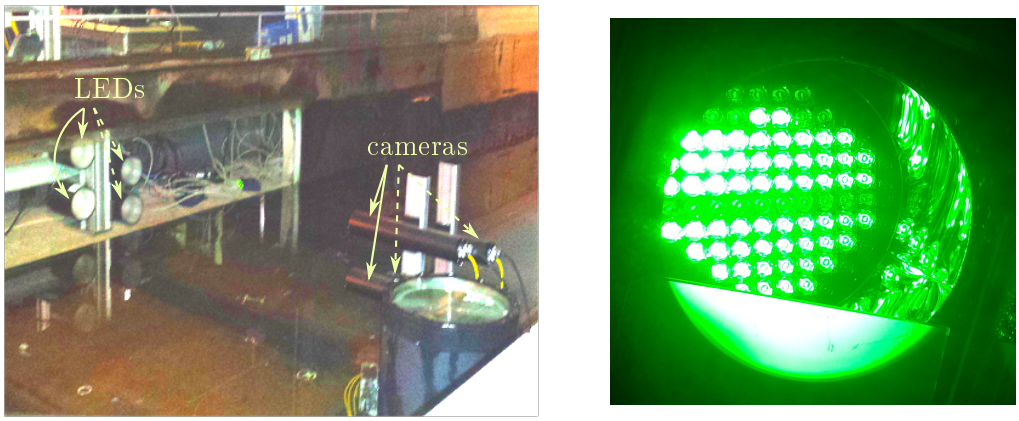

Figure 3.6.: Left: Cameras and LED light sources in the facility of Luminy. Dashed arrows indicate *cam*2 and *cam*3 and the respective light sources, which are not run for the whole campaign. Right: Light source for bubble illumination (with some defect LEDs). Here, LEDs are partly covered by a frosted glass screen. For experiments a screen is glued onto the cylinder.

Table 3.5.: Camera settings at Luminy for *cam*4. Height specifies the distance to the ground of the channel from the middle of FOV.

water	frame rate	field of view	t_{exp}	height	β
fresh/Butanol	200 Hz	1800 px x 978 px	$\approx 100\,\mu$s	50.5 cm	$1 : 2.12 \pm 0.01$

3.2.2. Calibration measurements

For depth calibration a grating with 500 l.p.i. (lines per inch), which equals to a grating distance of 51 µm, is used. Calibration pictures are taken in 50 µm steps adjusted by a micrometer screw. 200 pictures are taken covering a depth interval of 10 mm. Out of focus the depth dependent PSF is in the order of the grating distance, e.g. $\mathrm{d} = 5\,\mathrm{px} \cong 62\,\mu\mathrm{m}$. This means the used grating has too small grid spacing for depth calibration out of focus. It leads to smoothed intensities out of the focal plane, thus lower maximal and higher minimal intensities. Therefore the background factor f_{bg}, also applied at the calibration data, slightly corrects. Lacking alternatives the calibration data is used.

3.2.3. Measurement conditions

At Luminy optical bubble measurements are performed in two different heights, mentioned in sec. 3.2.1. The upper one is installed approximately 40 cm below the calm water surface. It would have been desirable to install them closer to the surface to enlarge the probability

of detecting bubbles. This was not possible due to restrictions by the channel geometry.

The camera and lens specifications used in Luminy are listed in tab. 3.4. Data of camera settings are presented in tab. 3.5. A trigger system, using an Arduino Uno, is installed to perform simultaneous measurements with the LHC. The Arduino receives the trigger input at a rate of f_0=100 Hzfrom a function generator and redistributes the signal to the LHC, the bubble cameras and the bubble light sources. All measurement techniques use different recording frequencies which can be deduced from f_0. Fig. 3.7 shows the trigger conditions for bubble and LHC measurements. For more details the work in progress of Bopp [3] is recommended. The magnification factor is determined by a chessboard pattern with squares of 2 mm x 2 mm . The exposure time t_{exp} is adapted to the light conditions so that the 8 bit range is fully used. The field of view is selected in such a way, that at a recording frequency of $f = 200$ Hz, continuous data transfer via an USB3 interface is possible.
The wind and water conditions measured at Luminy are listed in tab. 3.6. Friction velocities u_* are only available for fresh water measurements without additional wave paddle. Frequency and amplitude of the mechanical paddling is adjusted to obtain a two dimensional homogeneous wave field ($f_{\mathrm{pad}} = 0.9$ Hz, $A_{\mathrm{pad}} = 2$ V, $A^*_{\mathrm{pad}} = 1$ V) and most unstable breaking conditions ($f_{\mathrm{pad}} = 1.3$ Hz, $A_{\mathrm{pad}} = 2$ V). The significant wave height H_{s} is calculated by the wave deflection η, $H_{\mathrm{s}} = 4\sqrt{\eta^2}$. The dominant wave frequency f_{peak} adapts the paddle frequency for paddle conditions.

Table 3.6.: Wind and wave conditions in Marseille. Dominant wave frequency f_{peak} and significant wave height H_{s} from Bopp [3]. Friction velocity u_* from Kunz [20]. Wind speed $u_{10}(u_{\mathrm{ref}} = 10\,\mathrm{m\,s^{-1}})$ from unpublished data of K.Degreif (Heidelberg), data for $u_{10} = 12\,\mathrm{m\,s^{-1}}$ and $14\,\mathrm{m\,s^{-1}}$ is extrapolated.

u_{ref} in $\mathrm{m\,s^{-1}}$	u_{10} in $\mathrm{m\,s^{-1}}$	u_* in $\mathrm{cm\,s^{-1}}$	H_{s} in mm	f_{peak} in Hz	paddle
14	18.6	2.31	92	1.47	off
14	-	-	132	0.9*	on
14	-	-	233	0.9	on
14	-	-	130	1.3	on
12	15.5	1.59	75	1.93	off
12	-	-	188	0.9	on
10	12.6	1.66	58	1.52	off
10	-	-	161	0.9	on
10	-	-	119	1.3	on

Butanol

Butanol is added while mixing to obtain a well mixed water volume. Mixing is performed for the mass balance method, running a circulating pump to mix water into the water bulk, which is highly treated with gas. Thus, an uniform Butanol concentration can be assumed. Butanol is is added in two steps: before the experiments on the 22/06/2016, 6 l of Butanol are added. On the 23/06/2016 another 2.5 l of Butanol are added. From a water meter, the

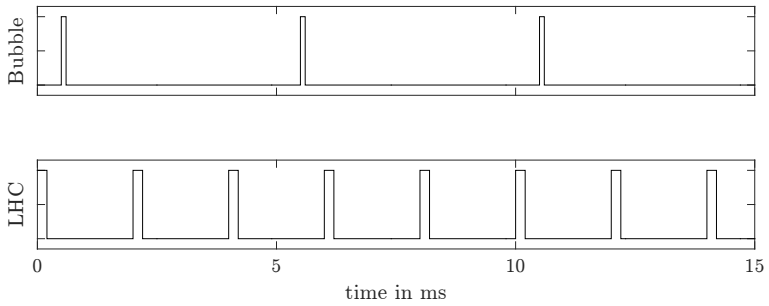

Figure 3.7.: Trigger conditions in Luminy. LHC with $t_{exp} = 200\,\mu s$ at $f = 500\,Hz$. Bubble set-up with $t_{exp} = 100\,\mu s$ at $f = 200\,Hz$.

total water volume in the channel is read to be $V = 125\,m^3$. Neglecting gas transfer, Butanol concentrations of c_1=48 ml m^{-3} (22/06/2016) and c_2=68 ml m^{-3} (23/06/2016) are reached.

3.3. Aeolotron - Heidelberg 2016

The Aeolotron at the Institute of Environmental Physics at Heidelberg University is an annular wind wave channel. It has a diameter of about 9 m, the width amounts to 60 cm and a common water height is 100 cm. Two wind engines generate reference wind speeds of up to 10 m s^{-1} resulting in water bulk velocities of about 20 cm s^{-1} and u_* is in the order of 3 cm s^{-1} [2]. The Aeolotron can be operated in an open and in a closed mode, referring to the air-side. This is of interest for mass balance methods. Several environmental parameters as temperature, humidity, wind speed and bulk velocity can be measured by probes.
During this measurement campaign other measurement techniques are applied simultaneously. Most relevant for this work is the LHC (see sec. 3.4.1) which provides the water-wave height and a mass balance technique measuring gas transfer rates (see sec. 3.4.2). For more detailed information about the Aeolotron and its components see Richter [25]. More information about the wind and water velocity fields is provided by Bopp [2].

3.3.1. Bubble measurement set-up

Measurements at the Aeolotron are taken in different heights. Therefore the light source and the camera system are mounted on a movable bar and in an as close as possible and fixed position. By moving the bar the measurement system is adjustable in height. Due to technical restrictions and limitations by the dimension of the channel a mirror is added to the system to realise the illumination. It has the same dimension as the measurement window and is stuck to the outer wall of the annular channel. Advantage of the mirror technique is, that no additional object is in the water, which influences water

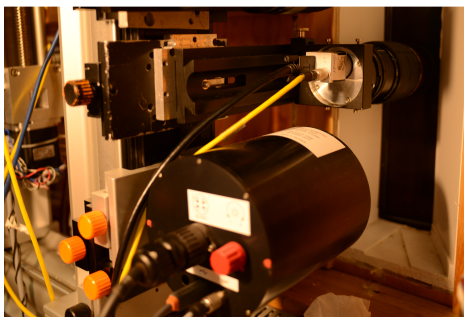

Figure 3.8.: Camera and light source.

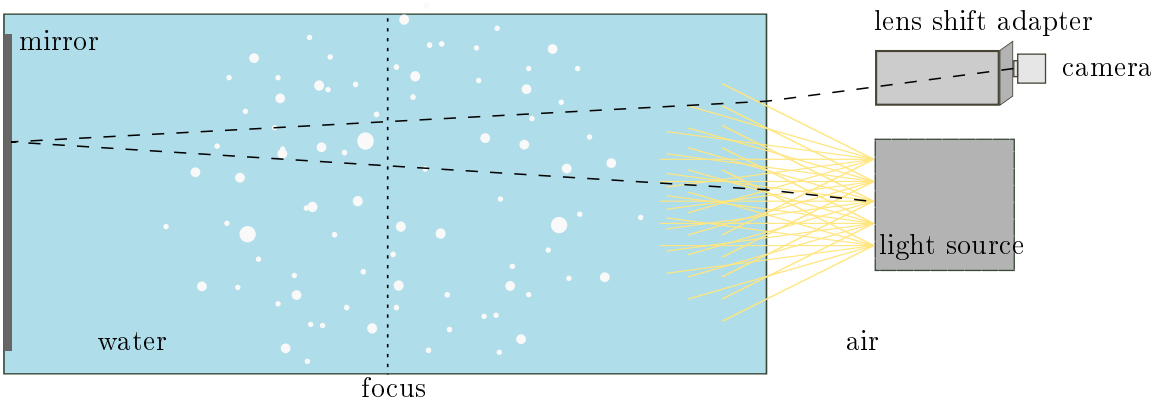

Figure 3.9.: Measurement set-up at the Aeolotron.

currents, except the flat mirror stuck to the wall.
A shift adapter for the camera lenses is necessary because of the slightly inclined light path via the mirror. The shift adapter shifts the lens system parallel to the sensor of the camera, enabling all optical elements being parallel. The inclination angle can be approximated by $\tan^{-1}(a/b)$ with $a \approx 5\,\text{cm}$ being half the vertical distance between camera and light source and $b \approx 60\,\text{cm}$ the width of the Aeolotron. This results in an inclination angle of $\alpha = 4.8°$. The angle is small enough to not influence the imaging quality noticeable. A sketch of the measurement set-up is shown in fig. 3.9.

Table 3.7.: Camera and lens specifications for bubble detection at the Aeolotron

acA1920 155um – Basler ace	
sensor typ	CMOS – sony IMX174
sensor size	11.3 mm x 7.1 mm 1920px x 1200px
pixel size	5.86 µm x 5.86 µm
lens system	f=105 mm vivitar series $n_f = 11$

3.3.2. Calibration measurements

Table 3.8.: Camera settings at the Aeolotron. Height specifies the distance to moving water surface during experiments.

experiment	frame rate	FOV	t_{exp}	height	β
VE water	200 Hz	600 px x 1000 px	100 µs	0 to 60 cm	$1 : 2.26 \pm 0.01$
VE + Butanol	200 Hz	600 px x 1000 px	100 µs	0 to 60 cm	$1 : 2.03 \pm 0.02$

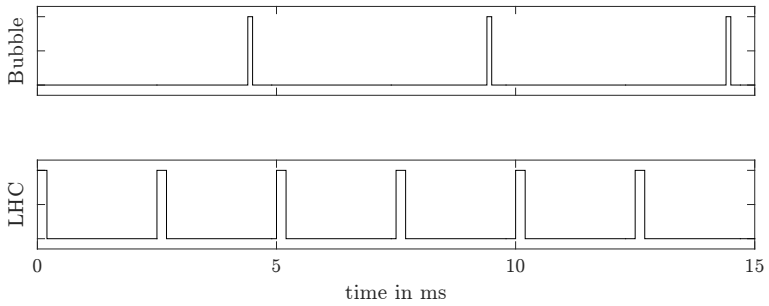

Figure 3.10.: Trigger conditions at the Aeolotron. LHC with $t_{\mathrm{exp}} = 200\,\mu\mathrm{s}$ at $f = 400\,\mathrm{Hz}$. Bubble set-up with $t_{\mathrm{exp}} = 200\,\mu\mathrm{s}$ at $f = 200\,\mathrm{Hz}$.

The basic idea of how to determine the measurement depth is explained in sec. 4.1.1. Hereafter, details of the calibration data and the used calibration target are described.
For fresh water measurements in October and November 2016 the same grating as for Luminy and Kyoto calibration measurements is used as target (with 500 l.p.i). Pictures in depth intervals of 50 µm are taken, covering an overall depth of 9 mm . The used grating is not an optimal calibration target since, out of focus, the depth dependent PSF (i.e. d = 5 px $\cong$ 66 µm) is in the order of the grating distance $\Delta \cong 51\,\mu\mathrm{m}$. Considering a background correction as described in sec. 2.2.1, the error gets reduced. Lacking alternative calibration data, this calibration is still used. For the Butanol measurements in December 2016 a perforated plate is used as the target due to its sharp edges. At each depth, 20 images are taken with an exposure time of $t_{\mathrm{exp}} = 100\,\mu\mathrm{s}$. Pictures out of focus are taken in 500 µm intervals. Close to the focal plane the interval is reduced to 100 µm.
The background correction and normalization is done in the same way as for bubble pictures, see sec. 2.2.1.

3.3.3. Measurement conditions

Camera and lens specifications are summarized in tab. 3.7. The camera settings, which are used for the experiments at the Aeolotron in autumn 2016, are listed in tab. 3.8. The exposure time t_{exp} is chosen such that the 8 bit range is almost filled out. In all experiments it is in the order of 100 µs. Bulk velocities of $20\,\mathrm{cm\,s^{-1}}$ are expected for the highest wind speed. This leads to possible smearing of 20 µm corresponding to about 1 to 2 pixels. This is of no concern for bubble detection. For the measurements in December 2016 a new calibration had to be done especially for the LHC, thus the camera system had to be readjusted. With the given pixel size and image dimension a field of view of 7.1 mm x 11.9 mm for the first measurements and 7.9 mm x 13.2 mm for the measurements with added Butanol in December 2016 is obtained.
How LHC and the bubble measuring system are triggered is depicted in fig. 3.10.
Measurements are performed at multiple wind and water conditions. The common reference for wind speed at the Aeolotron is the frequency of the wind generating fan f_{ref}. Bubble measurements are performed at the five highest standard frequencies of the wind generator, since only the high wind conditions lead to wave breaking and thus entrain bubbles. Values

for the calculated wind speed in 10 m height u_{10}, friction velocity u_*, the significant wave height H_s and the frequency of the largest dominant wave f_{peak} for the various conditions are given in tab. 3.9.

Table 3.9.: Wind and water conditions for measurements at the Aeolotron. * indicates Butanol conditions. f_{peak} is obtained by applying a low-pass frequency filter to the wave spectra calculated by the smoothed LHC data. It is an approximation for the lowest, highly developed wavelength. The data is provided by Bopp [3].

f_{ref} in Hz	u_{10} in $m\,s^{-1}$	$u_{*,w}$ in $cm\,s^{-1}$	H_s in mm	f_{peak} in Hz
19.9	8.20 ± 0.39	0.96 ± 0.06	91 ± 7	0.85 ± 0.03
19.9*	8.36 ± 0.40	0.99 ± 0.06	89 ± 7	0.87 ± 0.04
25.1	11.19 ± 0.49	1.46 ± 0.09	134 ± 10	0.72 ± 0.03
25.1*	11.19 ± 0.50	1.46 ± 0.09	134 ± 10	0.74 ± 0.03
31.5	14.27 ± 0.64	2.06 ± 0.13	183 ± 13	0.64 ± 0.03
31.5*	14.20 ± 0.65	2.04 ± 0.13	183 ± 13	0.68 ± 0.06
39.5	18.89 ± 0.72	3.10 ± 0.18	301 ± 19	0.51 ± 0.01
39.5*	18.59 ± 0.77	3.03 ± 0.19	302 ± 15	0.51 ± 0.01
50.0	22.63 ± 1.23	3.96 ± 0.29	321 ± 16	0.44 ± 0.01
50.0*	22.58 ± 1.28	3.95 ± 0.30	332 ± 18	0.44 ± 0.01

Butanol

Butanol is added to the water for simulating seawater conditions. Seawater has, due to its salt concentration, destructive properties for laboratory facilities. It is not yet explained why Butanol might have a similar effect on bubble formation as salt. One aim is to compare bubble spectra of Butanol water to those of salt water for an estimation whether it is a good alternative.
As Butanol was already used in Kyoto, concentrations are chosen in the same order of magnitude (initial concentration in Kyoto $c_{but} = 51\,ml\,m^{-3}$). In Heidelberg Butanol is added in two steps to not overdose. First, 500 ml are added to the large storage water tanks with a loading capacity of about $26\,m^3$. $18\,m^3$ of those are pumped into the Aeolotron. An by eye measurement implied a to little concentration for significant change in bubble formation. In a second step 500 ml are added to the $18\,m^3$ load in the facility, resulting in an initial Butanol concentration c_0.

$$c_0 = \frac{500\,ml}{26\,m^3} + \frac{500\,ml}{18\,m^3} = 19.23 ml\,m^{-3} + 27.78 ml\,m^{-3} = 47.01 ml\,m^{-3}$$

3.4. Complementary measuring techniques

Two measurement techniques, which are of importance for bubble measurements, are briefly described below. Simultaneous measurements of the different techniques are performed.

3.4.1. Laser height camera - LHC

The laser height camera allows a water-wave height measurement, using a fluorescent indicator namely Pyranine which is added to the water. A blue laser is reshaped to a sheet with a patch dimension of $A = 30\,\text{mm}$ x $2\,\text{mm}$, see Bopp [3]. Pyranine gets excited by the laser beam and subsequently emits at around $\lambda = 512\,\text{nm}$. This leads to a distinct gradient in intensity at the water surface and thus makes the water height detectable. The significant wave height H_s, a peak frequency f_peak, the height h and thereof a low-pass filtered phase can be obtained from the LHC data. This measuring technique is used in the measurement campaign at Luminy in June 2016 and at the Aeolotron in autumn 2016. For further information and more details about the detection algorithm of the water surface, see Schwarz [27].

3.4.2. Mass balance method

The basic idea behind the mass balance method as an evasion experiment is to load the water bulk with multiple trace gases by an oxygenator before the actual experiment starts, such that there is a concentration difference between water and air. Tracers in different orders of magnitude of solubility are used. By monitoring the tracers concentration in the water over time, after the wind is switched on, transfer velocities can be obtained. For concentration analysis a membrane inlet mass spectrometer (MIMS) is used. The method integrates over the whole water surface and has no spatial resolution. A box model is used for the calculations and challenges as the leak rate have to be factored into the mass balance equation. For further reading see Krall [18].

4. Data analysis and processing

This chapter is about data analysis and its processing. First, details about calibration are provided. The term 'height' describes a vertical distance, whereas 'depth' is a horizontal measure, mostly in the meaning depth of field for volume calibration. Information about how spectra are generated and how phase and height dependency can be evaluated is given. Moreover limiting factors in size determination are analysed and an approach on error estimation is revealed.

4.1. Calibration

Calibration of the collected data has to be performed at several points. First of all, the measurement volume has to be determined. Therefore knowledge about the magnification factor and the measurement depth is required, see sec. 4.1.1. For some data it is made use of the absolute distance to water surface, which has to be calibrated, see sec. 4.1.2.

4.1.1. Measurement volume

The measurement volume has to be specified to serve as a basis for density calculations. The field of view (FOV) and the depth of field (DOF) determine the measurement volume V.

$$V = \mathrm{FOV} \cdot \mathrm{DOF}$$

with [FOV]=m^2 and [DOF]=m.

Field of view

The FOV is known from the pixel dimensions and the magnification factor. How the latter is obtained, is written in the descriptions of the experiments, chap. 3. An object size dependent reduction of the FOV on all four sides is performed, since bubbles that extend beyond the full FOV are not considered.

Depth of field

It is challenging to determine the size dependent depth of field. How the calibration is realized for the present measurements is explained in the following.
The basic idea is to adjust a simulation of the calibration target, which includes the depth dependency, such that it fits best to the depth sequence of the calibration target. The relation between an object in the object plane and its image in the sensor plane is described by the point spread function (PSF), see sec. 2.1.

A model of the PSF consists of two parts, the diffraction part (PSF_{diff}), which depends on the optical set-up, and a depth dependent part ($PSF_{depth,i}$). Once the model PSF (=PSF_{diff} + PSF_{depth}) is extracted from the calibration data, it is applied to the bubble simulation. Depth information thus can be transferred to the bubble records.

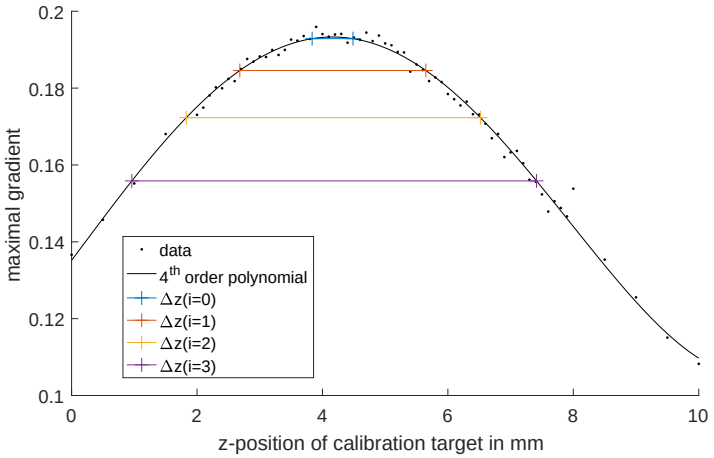

Figure 4.1.: Maximal gradients of O in the calibration picture series around the focal plane and 4^{th} order polynomial fit. The coloured lines indicate the DOF in depth i. Calibration data: Heidelberg, December 2016.

A sharp edged object O is used as a calibration target. A depth sequence of the object O is recorded. Maximal gradients of O for the depth sequence are depicted in fig. 4.1. The image of O is simulated by a two dimensional step function. Comparing the simulation and calibration sequence one can quantify PSF_{diff} and identify absolute depth for $PSF_{depth,i}$ as follows:

- **PSF_{diff}**: The PSF in the focal plane, caused by diffraction PSF_{diff}, can be approximated by a Gaussian filter G. To experimentally determine $\sigma(G)$, σ is adopted till the maximal gradient of the simulation equals the maximal gradient of the calibration data. In tab. 4.1 the theoretically calculated and experimentally determined σ for the different measuring campaigns are compared.

- **PSF_{depth}**: Depth dependent blurring is a result of objects being out of the focal plane. The depth dependent PSF_{depth} is realized by filters of the shape of the aperture [16]. It is approximated by a disk of which the radius increases with depth ($r(i=0)=0$ px, $r(i=1)=1.5$ px, $r(i=2)=2.5$ px), $r(i=3)=3.5$ px). These filters are applied to the simulated and with PSF_{diff} treated edge. Maximal gradients in the respective depth z_i are now identified with an absolute depth in fig. 4.1.

Now the relation between PSF(σ,z_i) and an absolute depth interval Δz is identified:

$$\Delta z(i=0) = 0.65\,\mathrm{mm}$$
$$\Delta z(i=1) = 2.97\,\mathrm{mm}$$
$$\Delta z(i=2) = 4.69\,\mathrm{mm}$$
$$\Delta z(i=3) = 6.45\,\mathrm{mm}$$

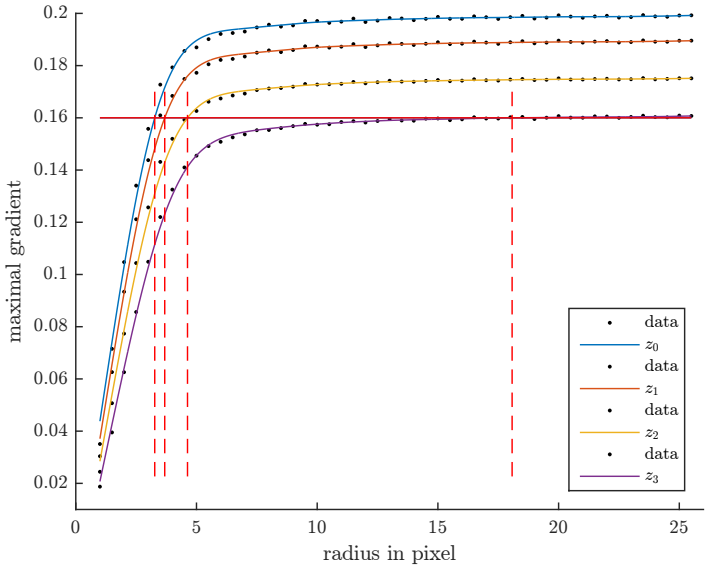

Figure 4.2.: Maximal gradient per radius of a bubble. Determined from a bubble simulation. PSF ($\sigma = 1.94$) of the Aeolotron data in december 2016 is applied. Additionally the depth dependent PSF is applied to the simulation and indicated as z_0 to z_3. The horizontal line represents the used gradient threshold of $g_\mathrm{thr} = 0.16$.

In the following the radius of the smallest bubble, still determinable in depth z_i, is identified. Therefore the model PSF is applied to a bubble simulation. This simulation consists of circles with radii of 1 px to 25.5 px in 0.5 px steps. The bubble detection algorithm uses a threshold in gradient g_thr to distinguish between focussed bubbles, which are taken into account, and unfocussed bubbles, which are considered as invalid. For the detection of small bubbles g_thr is a limiting factor. Fig. 4.2 shows the size dependent maximal gradient of bubbles in different depth $i = 0$ to $i = 3$. The radius where g_{thr} is reached, is the minimal detectable

bubble size r_{min} for the respective depth i:

$$r_{min}(i=0) = 18.07\,\text{px}$$
$$r_{min}(i=1) = 4.63\,\text{px}$$
$$r_{min}(i=2) = 3.68\,\text{px}$$
$$r_{min}(i=3) = 3.27\,\text{px}$$

The relation $\Delta z(r_{\min})$ extracted from the two relations $\Delta z(i)$ and $r_{\min}(i)$ is depicted in fig. 4.3. A continuous description of the size dependent depth of field is obtained by fitting a power series model of the form $a + b \cdot x^c$ to the resulting data points.

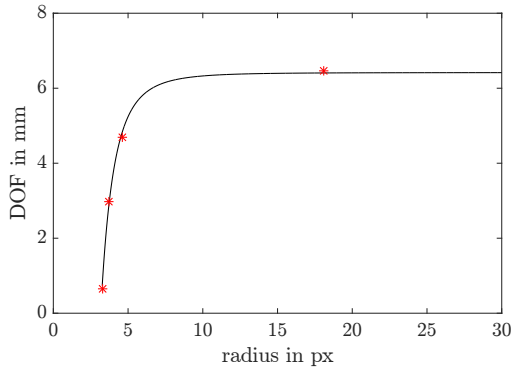

Figure 4.3.: Radius dependent depth of field $\text{DOF}(r) = \Delta z(r)$.

Some remarks on the depth sequence and the calibration target:

In fig. 4.1 the depth dependent maximal gradient is shown. The depth represents a relative measurement of distance. Pictures of a calibration target are taken in steps of 10 µm to 500 µm, details are written in the descriptions of the experiments in chapter 3. A similar normalization method as for the bubble pictures is used for the calibration pictures and an appropriate image section is selected. Appropriate basically means that only the central part is used, where the illumination is homogeneous. In the bubbles simulation the centres of the bubbles are in the middle of a pixel. A shift of the x- and y- coordinate of the centres leads to small changes in gradient of maximal $\pm 3 \cdot 10^{-3}$. Changes in gradient also dependent on whether the radius is an integer or a half-integer but not in a systematic way. A better calibration target would have contained bubbles, or holes, of different known sizes.

Compare sigma calculated to the experimental determination

Tab. 4.1 shows the maximal gradient detected in the calibration picture series and the respective σ_{exp} which is determined by discrete pixel filtering and the calculated σ_{calc} after (2.3), $\sigma = (\sqrt{2\pi} \cdot g_{\max})^{-1}$, with maximal gradient $g_{\max}$. Calculated sigma is always higher

Table 4.1.: Maximal gradient detected in calibration data for all four measurements. σ_{exp} is the experimentally determined σ used for a gaussian filter. σ_{calc} is calculated from eq. (2.3).

	max. gradient	g_{thr}	σ_{exp}	σ_{calc}
Kyoto 10.2015	0.23	0.17	1.56	1.73
Marseille 06.2016	0.31	0.25	1.03	1.29
Heidelberg 09.2016	0.28	0.16	1.20	1.42
Heidelberg 12.2016	0.19	0.16	1.94	2.10

than the experimentally determined one. Higher means broader and thus a smoother transition from bubble to background. An explanation is the discrete character of the Gaussian filter used for the experimentally determined σ_{exp}. Especially for small σ the discrete filter is a rough approximation of the Gaussian distribution. Furthermore the determination of discrete gradients (sec. 1.3.2) has a smoothing effect compared to the continuously calculated ones. Tab. 4.1 also lists the thresholds in gradient used for the various measurement campaigns. These values are defined experimentally.

4.1.2. Height calibration

A height calibration is necessary to get absolute distances between the wave height measurements and the bubble camera. This calibration is only used for the Heidelberg data set. LHC measurements are also available for Marseille, due to the very little bubble formation it is not applied yet. As indicated in fig. 4.4 the distance between the centre of FOV of the bubble measurements and the water surface is described by Δ.

$$\Delta(\eta, z_{\mathrm{R}}) = (z_0 - z_{\mathrm{R}}) + (\eta - \eta_0)$$

with η being the height data from the LHC. η_0 and z_0 are measured during calibration and represent the same absolute height in the respective coordinates. LHC data η is referred to the calibration target which is temporary fixed in the channel. The LHC data is provided by M. Bopp using [27]. z_{R} is the position of the bubble measuring system referred to a ruler which is fixed outside the channel at a X95 bar. To measure at different heights, z_{R} is varied. Two calibrations are performed, one for the measurements in October and November 2016 and one for the measurements in December 2016.

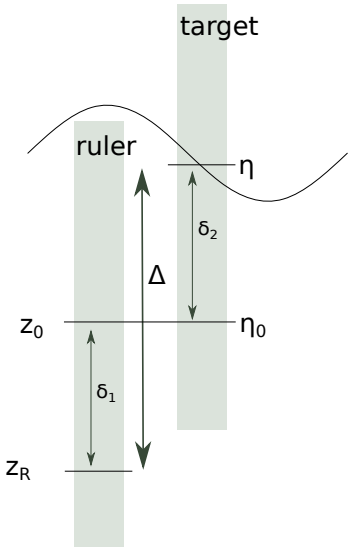

Figure 4.4.: Height calibration between the bubble measuring system and the LHC.

4.2. Representation of bubble spectra

For representation of bubble spectra usually histograms are used. How bin sizes are adapted and why a logarithmic scale is useful is explained in the following.
Small bubbles occur more frequently than larger ones. Bubble size distributions typically decrease exponentially with increasing radius. An increasing bin width leads to more bubbles counted for larger radii and better statistics. Thus, a logarithmic scale is the preferable option.
The boundaries of the intervals are given by $r_{\mathrm{i,edge}}$:

$$r_{\mathrm{i,edge}} = r_0 \cdot A^i \qquad \text{with } i \in [0, b] \tag{4.1}$$

The mean radius of the interval i is calculated by $r_{\mathrm{i,mean}}$:

$$r_{\mathrm{i,mean}} = r_0 \cdot A^{i+0.5} \qquad \text{with } i \in [0, b-1] \tag{4.2}$$

A free parameter is the number of bins b. 10 to 20 bins are common, depending on the probability density. The more bins, the less bubbles per interval are sorted and the larger is the statistical error, see sec. 4.3.2).
Furthermore the maximal and minimal radius $r_{\max}$ and $r_{\min}$, which are included in the histogram, have to be specified. $r_{\min}$ is reasonably chosen as the smallest detectable bubble. The limit due to size determination is decisive, a substantiated minimal radius is $r_{\min} = 3.5\,\mathrm{px}$. Maximal radii are in the order of 400 µm, which corresponds to about 30 px depending on the magnification factor.
The basis A is calculated by:

$$A = \left(\frac{r_{\max}}{r_{\min}}\right)^{1/b} \tag{4.3}$$

As mentioned above an exponential decrease of bubble density of the form $\Psi(r) = \Psi_0 \cdot r^{-s}$, is expected. In a logarithmic representation this results in a linear relation:

$$log(\Psi(r)) \propto -s \cdot log(r) \tag{4.4}$$

The slope s can be determined by a linear regression. This form of presentation is derived from Geißler [11].

4.3. Error estimations

4.3.1. Depth dependent magnification factor

The magnification factor is taken constant for the whole measurement volume. More correctly the determined factor is only valid in the focal plane where it is determined. Therefore the error resulting from bubbles, which are slightly out of focus, is estimated. Variables used in the following calculations are referred to the sketch in fig. 4.5.

$$m = \frac{B}{G} = \frac{b}{g} \quad , \qquad m' = \frac{B'}{G} = \frac{b}{g + \Delta z} \tag{4.5}$$

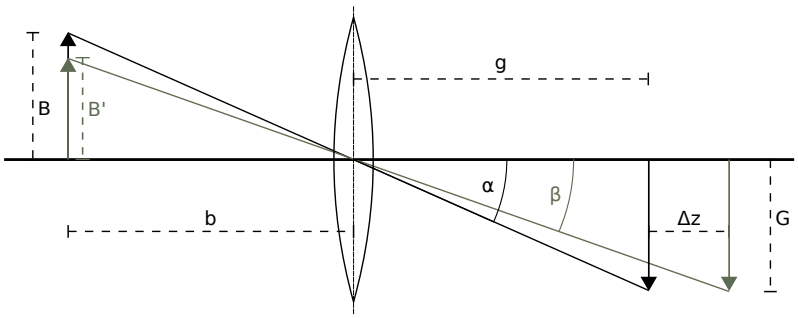

Figure 4.5.: b image distance, B image size, g object distance, G object size, Δz depth of field.

The image distance b is constant since the camera system is fixed. The relative error of the magnification factor f_m is calculated by:

$$f_\mathrm{m} = \frac{\Delta m'}{m} = \left(\frac{b}{g} - \frac{b}{g+\Delta z}\right) \cdot \frac{g}{b} = 1 - \frac{g}{g+\Delta z}$$

The following numbers enable a reasonable assessment of f_m: g in air in the Aeolotron is approximately 300 mm. Δz of 5 mm is reasonable.
This leads to a maximal relative error of $f_\mathrm{m} = 1 - \frac{300\,\mathrm{mm}}{305\,\mathrm{mm}} = 2\%$.

4.3.2. Statistical error of bubble density

The bubble density is calculated by eq. (4.6)

$$\Psi(r) = \frac{N(r)}{V(r) \cdot \Delta r} = \frac{N(r)}{\delta(r) \cdot A(r) \cdot n \cdot \Delta r} \tag{4.6}$$

with Ψ bubble density, N number of detected bubbles, δ depth of field, A field of view, n number of pictures and $\Delta r(r)$ the bin width of the histogram. The statistical error of N can be estimated by a binomial distribution. p is the probability to find a bubble of a specific size in a small volume V_i. Choose V_i such that p is very small. k is the number of V_i fitting into the whole measuring volume.
Expectation value μ and standard deviation σ for a binomial distribution are defined by:

$$\mu = k \cdot p$$
$$\sigma = \sqrt{k \cdot p \cdot (1-p)}$$

For small probability p the approximation$\sigma \approx \sqrt{\mu}$ is valid.
The standard deviation for the bubble density is determined by eq. (4.7):

$$\sigma(\Psi(r)) = \frac{\sqrt{N(r)}}{\delta(r) \cdot A(r) \cdot n \cdot \Delta r(r)}. \tag{4.7}$$

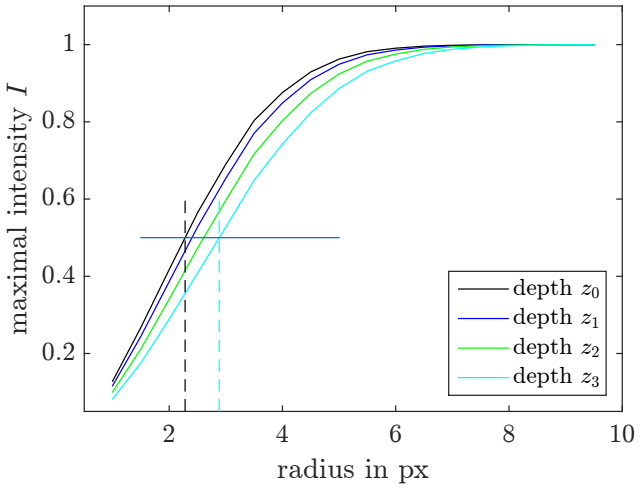

Figure 4.6.: Maximal intensity I of bubbles with radii of 1 px to 9.5 px in depth z_0 to z_3 in a.u.. The smallest bubble which can achieve intensity values of $I = 0.5$ has a radius of $r_{\text{min}} = 2.28\,px$. Graphs are obtained from bubble simulation for the campaign at the Aeolotron in December 2016, with $\sigma(PSF_{\text{diff}}) = 1.935$.

4.4. Limits in bubble detection

Bubble radii are determined using different thresholds and methods. Investigating those limiting factors one can find a lower limit in bubble size detection.

4.4.1. Intensity threshold

To label the objects of an image an intensity threshold at half maximum (= 0.5) is used. For small objects compared to the PSF, the maximum intensity decreases with depth. The maximal intensity I per radius and depth can be determined from a bubble simulation. Fig. 4.6 shows that the minimal detectable radius in the focal plane is $r = 2.28\,px$.

4.4.2. Gradient threshold

The gradient threshold g_{thr} is the crucial factor of validation of a bubble. From fig. 4.2, which plots the maximal gradient per radius and depth, the minimal detectable bubble in focus is identifiable with $r_{\text{min}} = 3.27\,px$. Fig. 4.2 is created with $\sigma(PSF_{\text{diff}}) = 1.935$ for the Aeolotron campaign in December 2016. This is the highest σ value of all campaigns (see tab. 4.1) and thus the upper estimate of r_{min}.

4.4.3. Size determination

A validation of the circle fit and the pixel counting method is done to estimate the limit in size determination. To compare the two methods of bubble size determination, a test pattern

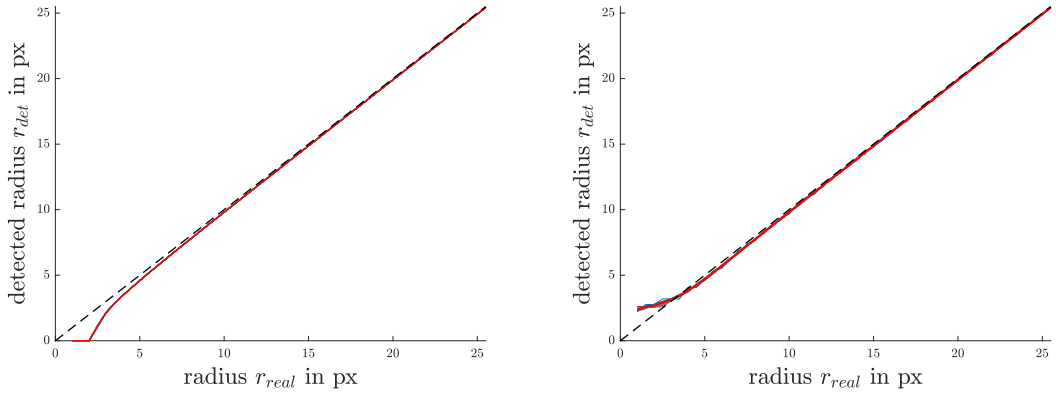

(a) **(b)**

Figure 4.7.: The size of simulated bubbles is determined by (a) circle fit, (b) pixel counting. Dashed line indicates the real size. Red line indicates the mean bubble size determined by the respective method. Thin multicoloured lines indicate size determinations with different shifts of x- and y- centre of the simulated bubbles.

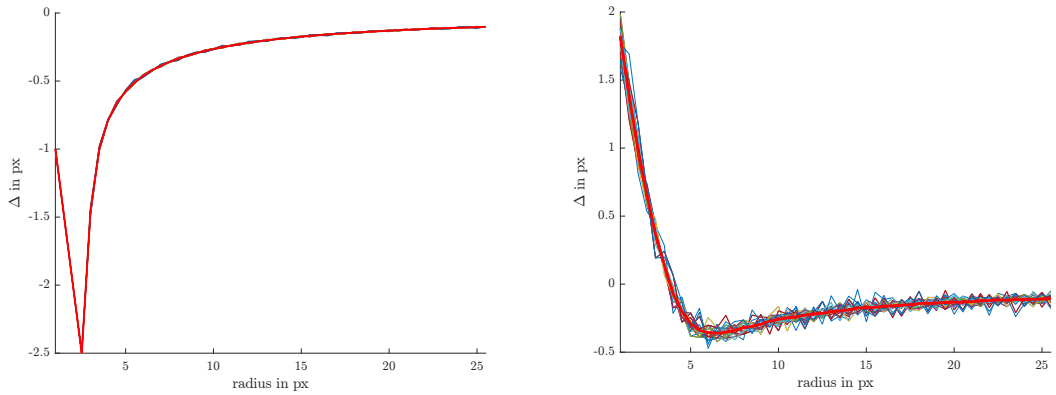

(a) **(b)**

Figure 4.8.: Validation of bubble radius determination . Δ represents the difference between the determined radius and the real radius. The mean of all detected sizes for a certain radius is marked with the thick red line. The different determination is a result of shifting the origin of the simulated bubbles. (a) radii are determined by the circle fit method .(b) radii are determined by pixel counting.

with bubbles of known sizes is created. The radii of the simulated bubbles vary between 1 px and 25.5 px. The simulation is run with different positions of the centres relative to the pixel grid. In the discrete representation the centres are shifted in 0.1 px steps in x- and y-directions. In fig. 4.7a and 4.7b the detected bubble size is plotted versus the real radius. Fig. 4.8a and 4.8b show the deviation Δ of the detected from the real radius ($r_{\mathrm{det}} - r_{\mathrm{real}}$). The multiple thinner lines represent the determinations for the different centre shifts. The mean of the determined size per simulated radius is drawn as thick red line. Except for the pixel counting method at very small bubbles, sizes are systematically underestimated with both methods. Due to strictly monotonically increasing of $r_{\mathrm{det}}(r_{\mathrm{real}})$ for radii > 2.5 px, it is possible to correct for the underestimation. The variance of detected sizes by pixel counting is larger as for the circle fit method. For a large number of detected bubbles the variance is still not relevant.

4.4.4. Result of different limitations

Limitations caused by the intensity threshold, the gradient threshold and by size determination are all in the order of 3 px. Different PSFs only slightly change values. As shown in fig. 4.8a and 4.8b the circle fit is less erroneous for smaller bubbles due to the higher slope. As a consequence the sizes determined by the circle fit are used, with a minimal radius of 3.5 px. The radii are corrected by $\Delta(r_{\mathrm{det}})$, shown in fig. 4.9.

$$r_{\mathrm{cor}}(r_{\mathrm{det}}) = r_{\mathrm{det}} + \Delta(r_{\mathrm{det}}) = r_{\mathrm{det}} + a \cdot r_{\mathrm{det}}^{b} \tag{4.8}$$

Table 4.2.: Correction coefficients a and b, depicted in eq. (4.8) and fig. 4.9.

	a	b
Kyoto 10.2015	1.213	-0.9907
Marseille 06.2016	0.5473	-0.9961
Heidelberg 09.2016	0.7395	-0.9989
Heidelberg 12.2016	1.803	-0.9814

The correction affects small bubbles the most. Small bubbles are only detected in the focal plane or very close. Thereof settings of the focal plane are used for the simulations. The diffraction part of PSF is depending on the measurement campaign. Data shown in sec. 4.4 (except fig. 4.9) is from Heidelberg in December 2016.

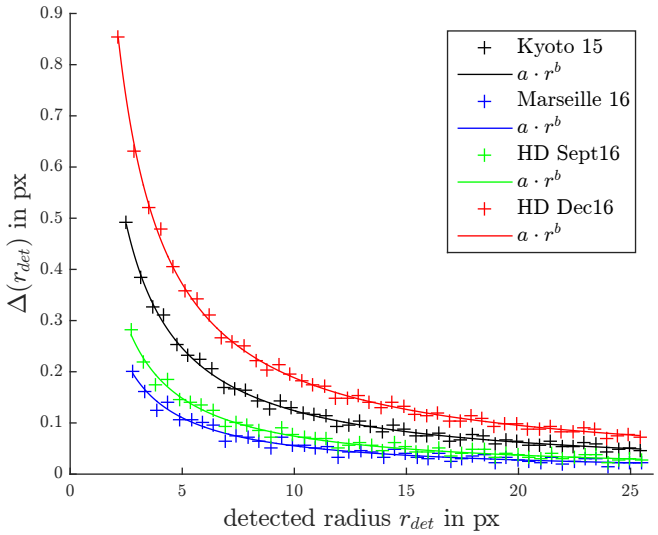

Figure 4.9.: Correction of radius size $\Delta(r_{\text{det}})$ for all campaigns. Variance between $\Delta(r_{\text{det}})$ is due to varying $\sigma(PSF_{\text{diff}})$.

4.5. Phase and height dependency

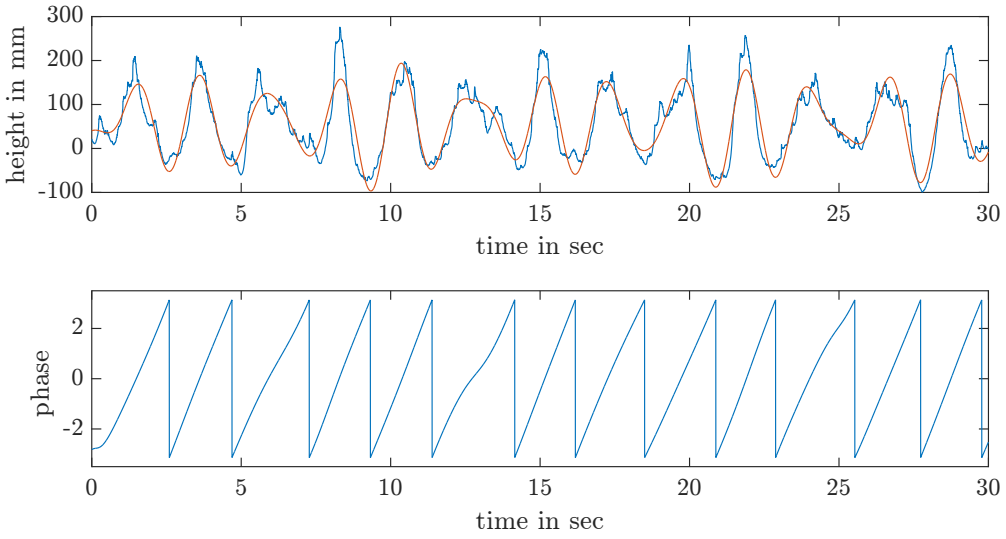

Figure 4.10.: Upper: Time serie of height. Blue: raw data. Red: low-pass filtered smoothed height. Lower: Phase values in the range $[-\pi, \pi]$. Height is given relative to a calibration height. Example from a measurement at the Aeolotron. 15.11.2016, at $f_{\text{ref}} = 50\,\text{Hz}$.

It is of great interest to analyse height and phase dependent bubble distributions and their characteristics. Measurements of the LHC provide height data of the same area as the bubble camera is focussed on. The LHC records at a frequency of 400 Hz at the Aeolotron in Heidelberg and 500 Hz at Luminy, Marseille. The LHC measurements are timed such, that the temporal delay to the bubble measurements is $< 1\,\text{ms}$. It is evident from fig. 4.10 that height and phase varies little over this time span and the LHC data and the bubble data can be considered as simultaneous measurements. Details about the trigger signals are to be found in fig. 3.10 for the Aeolotron and fig. 3.7 for Marseille. Height dependency is always expressed for a height interval of several cm so that the raw height data can be used. A height calibration that matches LHC and the height of the bubble measurement is applied, as described in 4.1.2. Phase dependence is reached by extracting the phase from the height data. Therefore the raw data is smoothed by a low-pass filter via Fourier transformation. The threshold of the low-pass filter is based on the peak frequency of the water waves. By means of a Hilbert transformation phase values in the range $[-\pi, \pi]$ can be extracted. The jump from π to $-\pi$ is an artefact of the periodicity of the phase.
Fig. 4.10 shows an example for the raw height data, the smoothed height and the obtained phase. Details about the LHC data and its processing will be published in Bopp [3].

5. Results and Discussion

Results of all measurement campaigns are presented concerning the goals mentioned in the beginning. Every facility has individual advantages and disadvantages. They depend on the wind conditions and the geometry of the facility. Limitations of the measurement technique are analysed.
The results of the measurement campaign in Marseille have to be treated with caution. The main reason for this is the increased amount of dirt particles in the water. Even thorough cleaning of the channel did not improve the situation. A distance to water surface of about 40 cm is the highest possible position for measurements. It is restricted by the measurement window. Wind conditions in Luminy, Marseille are in a rather low range. In general only little wave breaking happens, penetrating only low depth. Low bubble counting rates in combination with many particles in the tank amplify false positive detections and their weighting. Results of Marseille are shown in the appendix and some overview plots. In default of better data, u_* and u_{10} of the respective u_{ref} of fresh water measurements without additional paddle are taken for any kind of water and paddle condition, see tab. 3.6.

5.1. Bubble characteristics

Bubble spectra are analysed for the measurements at the Aeolotron and in Kyoto. Differences and similarities of both campaigns are pointed out.

5.1.1. Aeolotron Heidelberg

An extensive investigation of the height dependency of bubble appearance is possible at the Aeolotron.
The bubble measuring system is moved vertically to ten distinct positions with a spacing of 4 cm to investigate height dependency. Thereby an overall interval of 36 cm is covered. For a clear display several height positions are summarized in H_{i}:

H_1: 0.5 cm, 4.5 cm, 8.5 cm below calm surface.

H_2: 12.5 cm, 16.5 cm, 20.5 cm below calm surface.

H_3: 24.5 cm, 28.5 cm, 32.5 cm and 36.5 cm below calm surface.

Bubble size distributions $\Psi(r)$ of the different height intervals H_{i} for VE (deionized) water and Butanol conditions are depicted in fig. 5.1. Results of $f_{\mathrm{ref}} = 19.9$ Hz and 25.1 Hz can be found in the appendix. The size distributions are part in two regimes, distinguishable by different slopes in the log log plot. Linear fits, in the logarithmic representation, are given for appropriate radius ranges. The fits are weighted by the error of $\Psi(r)$ and described by the

slope α and β. Ranges are chosen manually with the aim to obtain little errors in the slope and an overlap within the range of both fits. Ranges are the same for one wind condition but may vary between VE and Butanol condition.
A dependency of bubble size distributions, also called bubble spectra, on the distance to water surface is observable, most pronounced at high wind conditions and large bubbles. In general, a decrease in bubble population with depth is observable for VE water and Butanol water measurements. Higher bubble densities for Butanol water are detected over all sizes and wind conditions.
Small bubbles (50 µm to 150 µm) show little depth dependency for the two highest wind conditions. They might be seen as an equilibrium background distribution. If there is no depth dependency, an equilibrium between the buoyant force, Stokes friction force and turbulence is reached. The upwelling buoyant force scales with $\propto r^3$, the force of friction with $\propto r^2$. Therefore larger bubbles rise faster and thus show a stronger depth dependence. A slight increase with wind condition of the radius where depth dependence starts can be seen in fig. 5.1. This is explicable by stronger turbulence at higher wind conditions. The stronger the turbulence is, the larger are bubbles in equilibrium.
As shown in fig. 5.1 only a weak depth dependence is observable at $f_{\mathrm{ref}} = 31.5\,\mathrm{Hz}$ over the full range of bubble sizes. Large errors and low densities indicate very low counting rates for large bubbles. Some of them might even be false positive detected objects, such as dirt or bacteria particles.
A closer look at the height dependency is possible by combining the bubble measurements with the wave height camera (LHC) data, see sec. 4.5. The following height intervals, which represent the absolute distance to water surface, are chosen to be interesting:

δ_1=0 cm to 2 cm

δ_2=2 cm to 5 cm

δ_3=5 cm to 10 cm

δ_4=10 cm to 15 cm

δ_5=15 cm to 60 cm

From fig. 5.2 it is evident, that the upper centimetres are the place where large bubbles, and even a significant higher concentration of small bubbles exist. Although there are restrictions by the measurement geometry by positioning the camera slightly above the measurement height, it is considerable that the resolution of bubbles in a distance of 0 cm to 2 cm below surface is possible.

A measure of penetration depth of bubbles might be the significant wave height H_{s}. From tab. 3.9, an enormous increase in H_{s} between $f_{\mathrm{ref}} = 31.5\,\mathrm{Hz}$ and 39.7 Hz is observable. The shape of the bubble spectra changes between those two wind conditions to higher bubble densities and a pronounced knee, as described above. Beneath the significant wave height, penetration depth of waves gives an estimation for the penetration depth of bubbles entrained by breaking waves. The penetration depth of a wave is defined as $\frac{\lambda}{2\pi}$, where λ is the

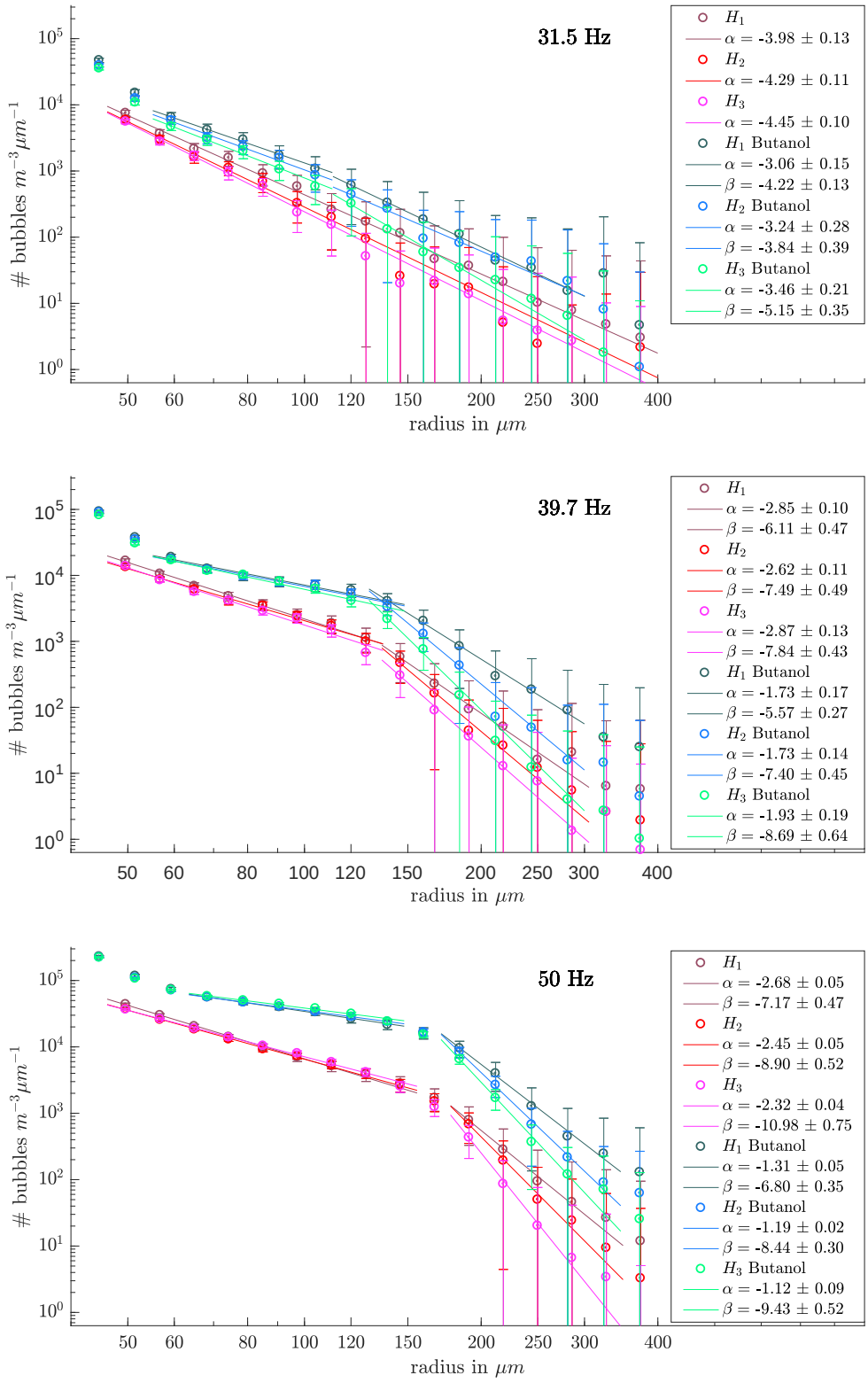

Figure 5.1.: Bubble distributions at wind conditions of $f_{\mathrm{ref}} = 31.5\,\mathrm{Hz}$, $f_{\mathrm{ref}} = 39.7\,\mathrm{Hz}$ and $f_{\mathrm{ref}} = 50\,\mathrm{Hz}$, for VE (deionized) water and Butanol conditions. The radius dependent bubble density is shown for three height intervals below water surface, H_1, H_2 and H_3.

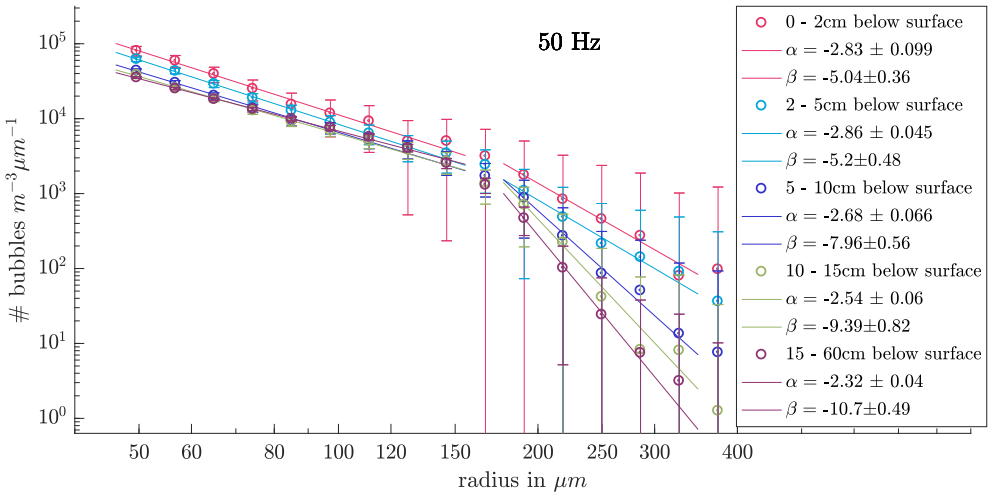

Figure 5.2.: Bubble density in various absolute distances to water surface with VE water at $f_{\mathrm{ref}} = 50\,\mathrm{Hz}$.

wavelength of the wave. The relation between wave frequency f and penetration depth z_{p} of a small amplitude wave is depicted in fig. 5.3. It can be derived from the dispersion relation for small amplitude gravity waves, formulated as [26]:

$$\omega(k) = \sqrt{gk \cdot tanh(k \cdot H)}$$

with angular frequency ω, wave number k, gravitational acceleration g and water depth H.

$$z_{\mathrm{p}}(f) = \frac{\lambda}{2 \cdot \pi} = \frac{1}{k} = \frac{\mathrm{g} \cdot tanh(k \cdot H)}{4 \cdot \pi^2 \cdot f^2}$$

Frequencies of the largest dominant wave and penetration depths are listed in tab. 5.1. In the present case of an annular facility, an additional water bulk velocity is expected, leading to a Doppler shift in the frequency measurement. Phase velocities are in the order of $\mathrm{m\,s^{-1}}$, bulk velocities in the order of $\mathrm{cm\,s^{-1}}$. Thus we measure systematically higher frequencies. Furthermore the approximation of small amplitude waves is technically not precise. It is not corrected for these deficiencies since only an estimation is needed. The penetration depth, in particular the stronger increase between $f_{\mathrm{ref}} = 31.5\,\mathrm{Hz}$ and 39.7 Hz, is consistent with increasing wave height and a different shape of the bubble distribution.

By means of the LHC a phase dependent resolution is possible. A phase dependency would be expected close to the water surface. Unfortunately no significant results are obtained. More bubbles tend to be in the wave trough but the statistic in 0 cm to 2 cm distance to the surface is not good an might even be biased by the measurement geometry.

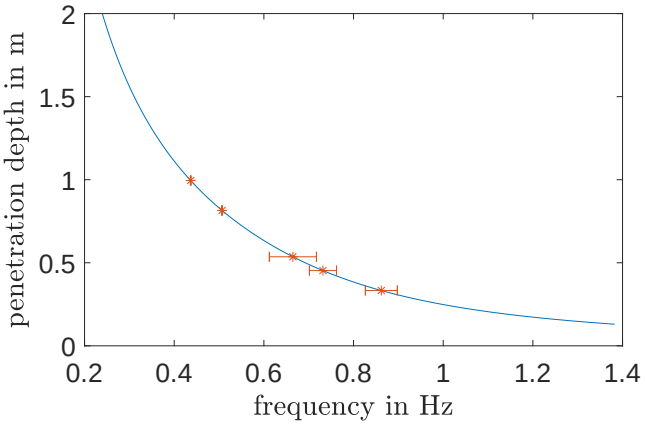

Figure 5.3.: Penetration depth $\lambda/2\pi$ in m vs. frequency in Hz as a result of the dispersion relation for small amplitude waves. This approximation is valid for amplitudes and wavelengths small compared to water depth [26].

Table 5.1.: Penetration depth z_p and dominant frequency f_peak of reference wind frequency f_ref at the Aeolotron.

f_ref in Hz	19.9	25.1	31.5	39.5	50.0
z_p in cm	33.3 ± 2.6	45.3 ± 3.5	53.6 ± 7.0	81.5 ± 0.1	99.5 ± 0.2
f_peak in Hz	0.85 ± 0.03	0.72 ± 0.03	0.64 ± 0.03	0.51 ± 0.03	0.44 ± 0.03

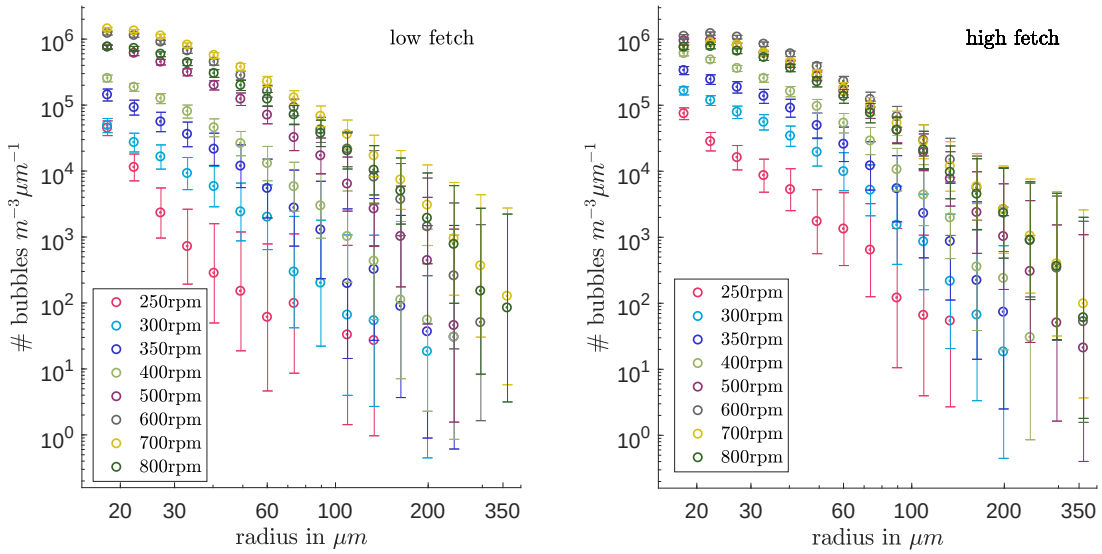

Figure 5.4.: Bubble size distributions of the Kyoto wind wave channel at different wind conditions for fresh water.

5.1.2. Kyoto

Major differences between the facilities in Kyoto and Heidelberg exist. The linearity of the Kyoto wind wave channel induces a limited fetch, meaning a limited area for wind acting on the water. Measurements are performed at 3 m ('low fetch') and 8 m ('high fetch') fetch. In general an increase of bubbles with fetch is expected. Fresh water in Kyoto is common tap water whereas VE (deionized) water is used in Heidelberg. How this influences bubble formation is unclear.

The shape of the spectra of Heidelberg and Kyoto are similar and an increasing slope with radius is obtained in both facilities. As shown in fig. 5.4, a significant increase in bubble appearance with increasing wind condition is observable for low and high fetch up to $f_{\mathrm{ref}} = 500\,rpm$. The stagnation in increase, which is more pronounced at the high fetch, is surprising. The knee at a rather distinct radius, where an abrupt change of the slope is observed as in Heidelberg, is not observable in Kyoto. It could be an effect of the channel's linearity and fetch dependency. The limited fetch might explain that a kind of equilibrium condition, where small bubbles are equally distributed in the whole water bulk, is never reached.

Especially at high wind speeds many bubbles colour the water whitish, leading to an overall intensity reduction of the background. The background intensity should be close to zero in the inverted and normalized image. A reduction of the illumination leads to a higher background intensity, see fig. 5.5, directly influencing gradients in the images at the bubbles' edge. Small bubbles are affected first, which explains the slight decrease in bubble density for the smallest bubbles.

The condition at $f_{\mathrm{ref}} = 800$ rpm is taken with changed water conditions. Due to the high water loss at the end of the channel, an additional pumping system is installed. For wind

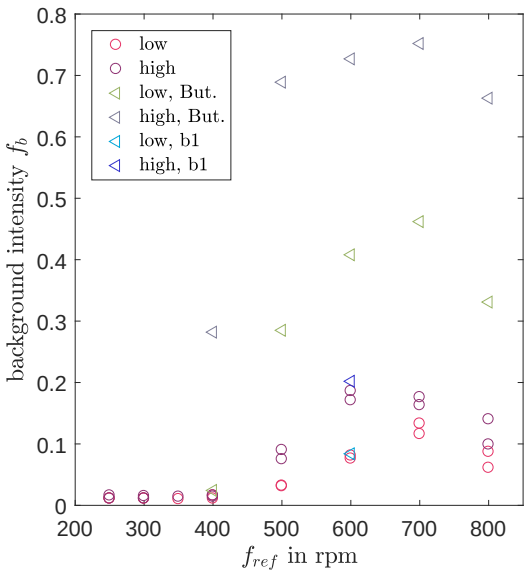

Figure 5.5.: Background intensity due to scattering bubbles vs. wind speed in f_{ref}. Calculated by the center of mass μ_{min} in the normalized and inverted image I, and min, the absolute minimum in I. $f_{\mathrm{b}} = \frac{\mu_{\mathrm{min}}+min}{2}$.

speeds up to $f_{\mathrm{ref}} = 700\,\mathrm{rpm}$, fresh water is pumped into the channel at the wind entrance, which reduces the water loss. The described water addition is not sufficient at $f_{\mathrm{ref}} = 800\,\mathrm{rpm}$ such that a different pumping system is installed. The latter pumps water out of the channel at the channels end and into the channel at the wind entrance. Less water is pumped out than in. It is most likely that it influences bubbles spectra, but the concrete influence is speculative.

5.2. Butanol addition as seawater simulation

The main difference between seawater and fresh or deionized (VE) water is its ion concentration, namely NaCl. The influence of salts on bubble formation processes is complex and not yet well understood. Some effects are discussed by Craig [7]. One can argue with the repelling behaviour of ions. Ions stuck to the bubble surface inhibit bubble coalescence. As a consequence of this simplified model more small bubbles are expected. Butanol is a primary alcohol with the chemical structure $C_4H_{10}O$. It was discovered by hazard that it influences bubble formation in a similar way as salt.
Comparing bubble size distributions in fresh/deionized water and water with added Butanol will reveal new insights into the impact of Butanol. Initial Butanol concentrations of about 47 - 68 $\mathrm{ml\,m^{-3}}$ are used.
Butanol concentrations are monitored by a mass spectrometer. An expected decrease in concentration during a measurement, but an overall increase in Butanol concentration between measurement cycles (time spans of hours to days) is observed by the spectrometer. The increase is not explicable and it is understood as an artefact of the mass spectrometer which can not yet be explained. The temporal evolution of the measured Butanol concentration of the measurements in Heidelberg is shown in the appendix.

5.2.1. Aeolotron Heidelberg

Bubble distributions shown in fig. 5.6 are summarized over all heights for the measured wind conditions. Similar colors represent the same wind condition with VE water and Butanol water.
Some aspects in bubble spectra are significantly different for Butanol and fresh water. At the Butanol conditions more bubbles are observable over all bubble radii. The enhanced bubble appearance increases with increasing wind. The increase in bubble density at low wind conditions is in the order of a factor 3/2, for the highest wind conditions an increase by a factor of 10 is observable. The systematic increase of small bubbles ($< 65\,\mu\mathrm{m}$) is observed for Butanol conditions and not for VE water. The presumption that more small bubbles are present can be confirmed. It is explained either by initial formation or by prevention from coalescence, most likely both. One could expect enhanced turbulence due to the larger number of bubbles, which mix the water while rising. But the qualitative argumentation that the radius at the knee of the spectra depends on the strength of turbulence supports the conclusion that turbulence is not changed by the additive Butanol, as the position of the knee does not change significantly with Butanol.

Variation of Butanol concentrations

Since the mass spectrometer does not provide reliable concentrations, the effect of a changing concentration over time is estimated by a reference measurement. The condition at 50 Hz is the first measured Butanol condition. After all regular wind conditions are performed, another four heights at a condition of 50 Hz are performed. Distributions of both measurements are shown in fig. 5.7. A slight decrease in bubble formation over time can be stated. The characteristics of both measurements are still the same. Butanol concentration is assumed to be sufficiently constant for the measurements at the Aeolotron.

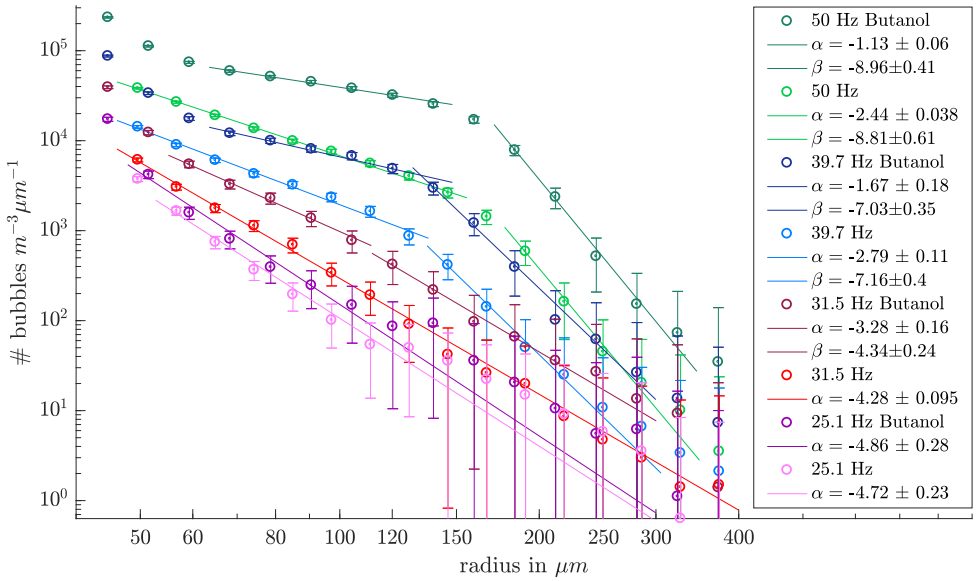

Figure 5.6.: Bubble distributions at multiple wind conditions given in reference frequency f_{ref}.

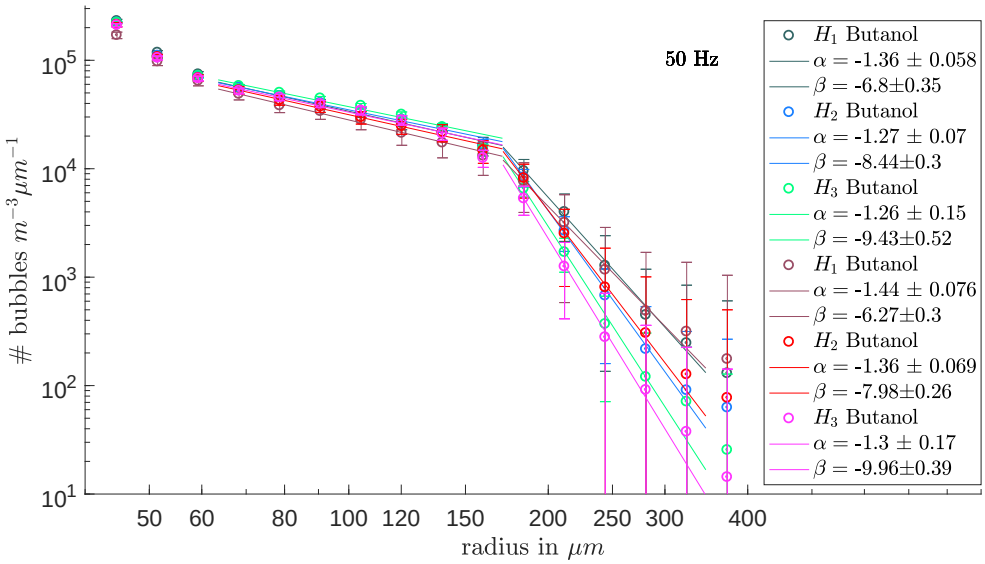

Figure 5.7.: Bubble size distributions for Butanol water measurements at 50 Hz. blue/greenish data is measured directly after Butanol is added to the water and well mixed. Redish data is measured two days later, after five complete conditions are measured. A slight decrease in bubble formation can be seen, explained by a reduction in Butanol concentration due to gas exchange.

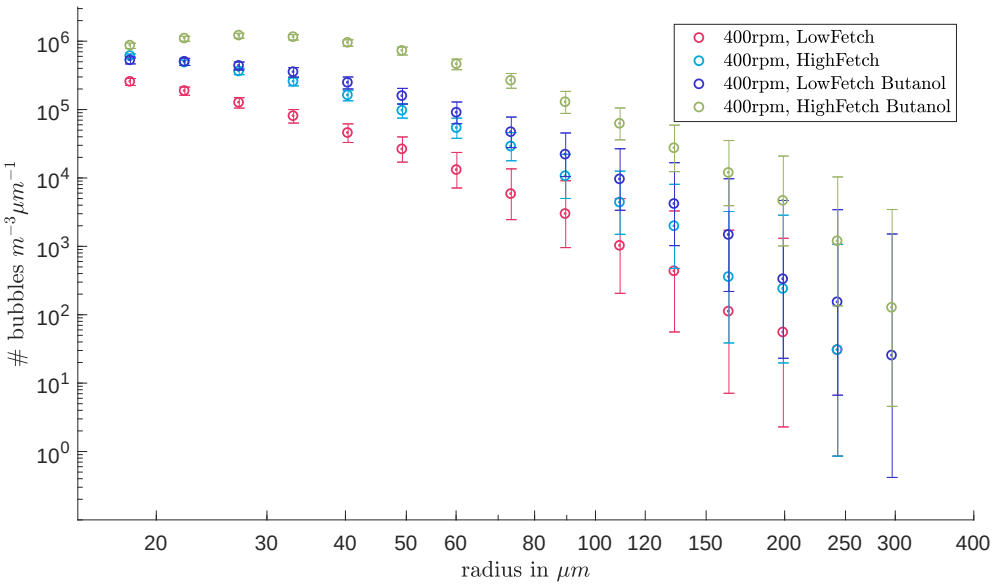

Figure 5.8.: Bubble size distribution for various water and fetch conditions at $f_{\text{ref}} = 400\,rpm$ in Kyoto.

5.2.2. Kyoto

At the measured conditions many bubbles form, such that an intensity reduction of the illuminating light of up to 75% is determined, see fig. 5.5. A background reduction influences the bubble detection directly and affects small bubbles first. Fig. 5.8 shows bubble spectra at $f_{\text{ref}} = 400\,\text{rpm}$, which is the lowest wind condition for Butanol measurements in Kyoto. Fresh water and Butanol conditions are depicted. Higher bubble densities are observed at the high fetch and for Butanol conditions. An indication for the limits in precise bubble detection at Butanol conditions are the decreasing bubble densities for small bubbles. From measurements in the Aeolotron and the primary assumption of the impact of Butanol, we would expect an increase, especially for small bubbles. It is explained by a systematic under detection of small bubbles at conditions which significantly reduce background illumination. The larger the reduction of the background the larger are the affected bubbles. Results of the Butanol measurements in Kyoto at high fetch are not meaningful, except the lowest wind condition at $f_{\text{ref}} = 400\,\text{rpm}$. Bubble detection at the low fetch, is limited reliable. It would have been interesting to have Butanol data from lower wind speeds.

5.3. Bubble effect on gas transfer

A qualitative analysis of the influence of bubbles for high and low soluble gases is performed. The exchange time τ_{ex}, which is the time until equilibrium in the bubble is reached, is of interest.

$$\tau_{\mathrm{ex}} = \frac{r}{3 \cdot \alpha \cdot k_{\mathrm{b}}(r)}$$

r is the bubble radius, α the dimensionless solubility and $k_{\mathrm{b}}(r)$ the transfer velocity of a single bubble. Solubilities can be estimated as 'high' for values much higher than 10, and 'low' for values much lower than 10, Mischler [23].

High solubility

Gases with high solubility quickly reach equilibrium. The volume of air entrained by breaking waves is the decisive factor. In a first approximation the whole bubble equilibrates and the total bubble volume participates at the gas exchange. A common representation of the bubble volume is the void fraction. Void fraction is a dimensionless number giving the ratio of air volume per water volume. The void fraction p is calculated from the bubble size distribution $\Psi(r)$.

$$p = \sum_{i=1}^{b} \frac{4}{3} \pi r_{\mathrm{i}}^3 \cdot \Psi(r_{\mathrm{i}}) \cdot \Delta(r_{\mathrm{i}})$$

with the mean radius of bin i r_{i}, number of bins b, the bubble spectrum $\Psi(r_{\mathrm{i}})$ and the bin size $\Delta(r)$.
Large errors are obtained due to the large errors in bubble densities, especially for large bubbles. A more realistic estimation of upper and lower limits of the calculated void fraction is by a relative error. With the relative error $\delta\Psi = \frac{\sigma}{\Psi}$ the upper and lower limits $p_{+/-}(r)$ are calculated by:

$$p_{+}(r) = p(r) \cdot (1 + \delta\Psi(r)) \qquad \text{and} \qquad p_{-}(r) = p(r) \cdot (\frac{1}{1 + \delta\Psi(r)}). \tag{5.1}$$

Low solubility

The bubble surface acts in a first approximation as an additional interface. This is valid especially for tracers of low solubility. Equilibration takes longer for those gases such that the surface acts longer as an additional exchange interface.
The ratio between the water surface and the bubble surface gives an estimation of the relevance of bubbles in gas exchange. The water surface gets enlarged by waves. An enlargement factor is hard to calculate and is certainly dependent on various parameters. The calm water surface of the respective facility is therefore used as reference.
The area fraction, abbreviated by q, is calculated from the bubble size distribution $\Psi(r)$ of the respective condition, with the facility specific water height H.

$$q = \sum_{\mathrm{i}=1}^{b} 4\pi r_{\mathrm{i}}^2 \cdot \Psi(r_{\mathrm{i}}) \cdot \Delta(r_{\mathrm{i}}) \cdot H$$

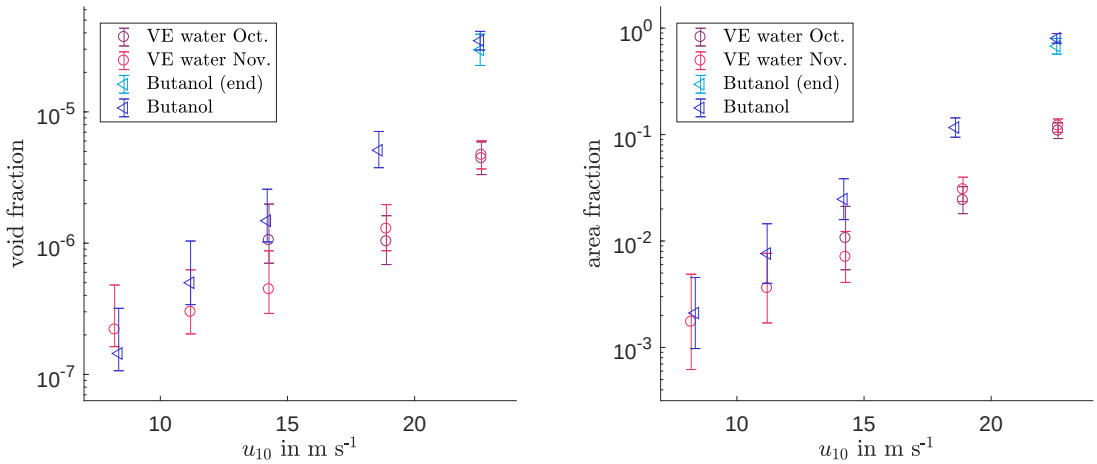

Figure 5.9.: Void fraction (left) and area fraction (right) at the Aeolotron. Measurements with VE (deionized) water and under Butanol conditions are depicted. During the campaign in October it is likely that bacteria influenced the measurements.

The error of q is determined in accordance to eq. (5.1).

5.3.1. Aeolotron Heidelberg

As shown in the logarithmic plot in fig. 5.9, the void fraction p increases with wind speed u_{10}. The wind conditions do not reach the regime where bubble mediated gas transfer is supposed to play a major role. Nevertheless a significant increase in bubbles is observable over the measured conditions. Void fraction is very low for the measured conditions. This indicates that bubbles are negligible for tracers with high solubility for the measured conditions.
As can be seen from fig. 5.9, at the highest wind conditions bubble surface reaches the order of the calm water surface. An overall bubble surface of the same size as the flat water surface might increase gas transfer by a factor of two. This conclusion is only valid in the approximation for low solubility.

5.3.2. Kyoto

The shape of void fraction and area fraction is similar. An increasing void fraction and area fraction with wind speed for fresh water is observed and shown in fig. 5.10.
Butanol data is also depicted and, as argued with the intensity reduction, does not represent what is seen by eye during the experiments. The spectral analysis showed that at $f_{\mathrm{ref}} = 400\,\mathrm{rpm}$ ($u_{10} = 40.7\,\mathrm{m\,s^{-1}}$) reasonable bubble detection is possible for Butanol conditions. This is reflected in the fractions: void and area fractions with Butanol are enlarged by factors 4 to 10, the increase tends to be larger at the high fetch. A closer look at the low fetch Butanol condition implies, that they are not as bad as described before, also by taking the background conditions as indication.
Fresh water, which is conventional tap water, shows an interesting behaviour for high wind speeds. The slope of void and area fraction decreases and a saturation is observable. The

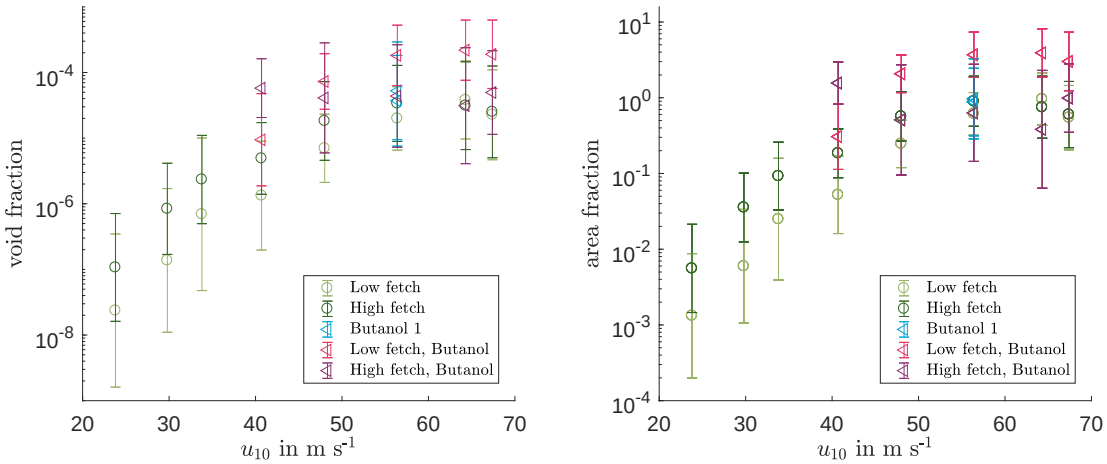

Figure 5.10.: Void and area fraction for the various measurements in Kyoto. Circles represent fresh water conditions, triangles indicate Butanol conditions.

saturation implies, that from wind speeds of about $u_{10} = 60\,\mathrm{m\,s^{-1}}$ on, no additional bubble formation is present. Bubbles form when waves are breaking. For even higher wind conditions the assumption is made that waves do not break any more but rather water patches get torn off and large amounts of spray are produced. The highest measured wind condition is questionable due to the additional water pumping, as mentioned above.

5.4. Discussion of the results

In the following an evaluation of possible errors and there influence on bubble spectra, void fractions and area fractions is performed. The depth calibration (DOF), see sec. 4.1.1, is the most questionable error source and might lead to systematic errors. As described in sec. 3, a more suitable calibration target could be used. The DOF changes the volume and thus bubble densities only linear reciprocally. A maximal error of factor 2 in DOF for measurements in Heidelberg and Marseille is estimated. Bubble size, wind and water condition dependencies and the general shape of $\Psi(r)$, $p(u_{10})$ and $q(u_{10})$ would be barely effected.
Particularly the calibration for the Kyoto data is critical, since it is done with a rebuilt set-up in Heidelberg. Furthermore high bubble densities are challenging in detection. The developed and applied drift correction (sec. 2.2.2) enables bubble detection for those strong conditions. How the drift correction influences the measurement volume is not investigated within this thesis. In fig. 5.11 the depicted data of all campaigns is measured in about 30 cm distance to water surface. Area fractions p are calculated with the assumption of constant bubble density over the whole water column. This assumption might be correct for small bubbles. A first estimation of the penetration depth of bubbles could be the penetration depth of deep water waves, which is dependent on the dominant wave frequency and water depth. Wave frequencies are not available for the Kyoto data. Water depth in Heidelberg is about 1 m and Marseille 0.9 m. Referring to fig. 5.3, which displays the frequency dependence

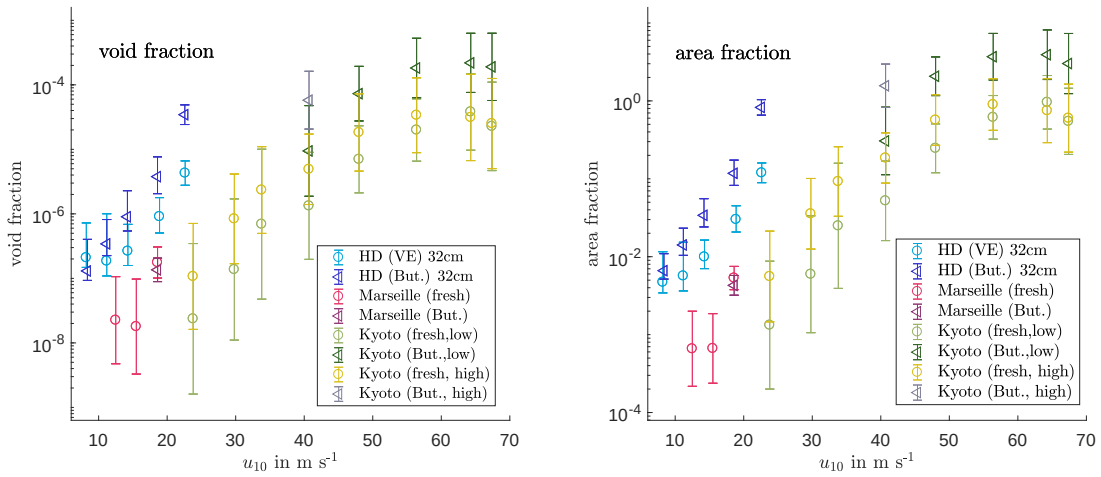

Figure 5.11.: Void and area fraction for the various measurement campaigns in Heidelberg (blue), Marseille (red) and Kyoto (green).

of penetration depth in Heidelberg, and the knowledge, that dominant wave frequencies in Marseille are in the order of 1.5 Hz (tab. 3.6), penetration depths in Marseille of about 15 cm are estimated. Evaluations of the height dependent data at the Aeolotron imply only little height dependence of void and area fractions. Whether the measurement height in Marseille at 40 cm below surface represents the mean in bubble density is hard to estimate.
Systematic errors would shift fractions of all conditions up or down. Only little influence on the shape of bubble spectra and thus void and area fraction is expected. As a conclusion, absolute values for Ψ, p and q have to be treated with caution. The wind speed and depth dependency within one campaign and the general shape of bubble distributions are meaningful. In particular fresh water measurements and their fetch dependency are reliable. The saturation effect, which is observed for fresh water measurements at both fetches, and measurements at the low fetch for Butanol conditions, is assumed to be true. For verification of the effect, further studies are needed.

6. Conclusion and Outlook

By means of the adapted algorithm of Mischler [22], bubble imaging data is evaluated from three different laboratory facilities in Heidelberg, Kyoto and Marseille. Special emphasis is placed on:

- Bubble characteristics of three wind-wave channels.
- The effect of low Butanol concentrations in fresh water as a substitute for seawater.
- The fetch dependency of bubble occurrence.

6.1. Conclusion

With the verified and adapted algorithm of Mischler [22] precise bubble detection is possible for various wind and water conditions. The lower detection limit of the applied method is at radii of 3.5 px, see sec. 4.4. Depending on the set-up components and the magnification factor, bubbles sizes of r_{min} =,18.2 µm in Kyoto, $r_{\mathrm{min}} = 46.6\,\mu\mathrm{m}$ in Marseille and $r_{\mathrm{min}} = 44.7\,\mu\mathrm{m}$ in Heidelberg are detectable (sec. 3). Changing illumination conditions, which occur by redirecting the background illumination via a slightly moving mirror or due to the amount of bubbles, are addressed. Dirt particles represent a challenge for automated bubble detection. For small particles which have a symmetric round shape - which look like bubbles - it is hard to find bubble specific properties which might improve the algorithm. In particular for little counting rates, as it is the case for large bubbles, dirt particles that are detected as bubbles might bias the spectrum. At wind and water conditions which darken the background due to the amount of bubbles, precise detection in particular of small bubbles is limited. The critical regime depends on fetch, wind speed and whether fresh or Butanol conditions are investigated.

Butanol The study has shown that initial Butanol concentrations of about $c_0 = 48\,\mathrm{ml\,m^{-3}}$ to c_0 =$68\,\mathrm{ml\,m^{-3}}$ enhance bubble formation significantly. Typically void fractions and area fractions are raised by a factor of 3 to 10 with the existence of Butanol. At higher wind speeds the increase tends to be larger. Increasing bubble density is also visible in the spectra. An above-average augmentation is observed for small bubbles with $r_{\mathrm{bub}} < 65\,\mu\mathrm{m}$ in the Heidelberg measurements. No details about the effect of changing Butanol concentrations are known. At high wind conditions it is likely that concentrations change significantly in a time span which is relevant for measurements. From the Heidelberg measurements, with a maximal wind speed of $u_{10} = 22.5\,\mathrm{m\,s^{-1}}$, a slight decrease in concentration over two days and multiple measurement cycles is shown, which does influence the bubble occurrence.

Bubble surface. For the *Marseille* facility bubble concentrations are too low, to contribute considerably to gas exchange. At highest wind conditions in *Heidelberg*, bubble surfaces are in the order of 10% of the calm water surface for fresh water and 100% for Butanol conditions. An increase in gas transfer by bubbles for low soluble gases by a factor of two would thus be the upper limit of bubble influence in Heidelberg. *Kyoto*, with its hurricane like wind conditions, reaches bubble surfaces in the same order as the water surface, already for fresh water conditions. The bubble effect on gas transfer in fresh water thus should be similar to the effect under Butanol conditions in Heidelberg. Results at the low fetch in Kyoto and the results of Heidelberg prove the assumption of higher bubble formation under Butanol conditions.

Bubble volume. At Heidelberg and Kyoto the void fraction, which is decisive for high soluble tracers, is in the order of 10^{-8} to 10^{-4}. This is rather small compared to Deane and Stokes [8], who observed void fractions in oceanic bubble plumes in the order of 10^{-2} (30 cm below whitecaps). This is explicable by the detected bubble sizes, which are much smaller as in [8]. It is questioning whether larger bubbles than 400 µm do not appear in the measured facilities or are just not detectable by the applied method.

Fetch dependence. A strong fetch dependency of bubble appearance is observed, comparing three laboratory facilities. Similar bubble concentrations are counted in Kyoto as at the Aeolotron only for significantly higher wind conditions. Measurement positions in Kyoto are at 3 m and 8 m fetch, the annular geometry of the Aeolotron implies infinite fetch.

An expected sharp increase in bubble formation at wind speeds around $u_{10} = 35\,\mathrm{m\,s^{-1}}$ could not be observed . For hurricane like wind conditions at Butanol conditions, bubble detection is not reliable with this optical method.
Comparing the results of all campaigns a surprising finding is made. Kyoto implies a saturation in bubble appearance at wind speeds above $u_{10} = 60\,\mathrm{m\,s^{-1}}$. It seems reasonable with the following explanation: Wind forces waves to break, thereby bubbles get entrained. From certain high wind speeds on water gets torn away from the surface and no more increase in bubble formation is present. Even a decrease in bubble formation is conceivable.

6.2. Outlook

Results of Heidelberg show a change in bubble spectra with Butanol as it is assumed for seawater. A comparison of Butanol spectra to real seawater spectra is necessary for a better assessment of the impact of Butanol. Furthermore an analysis about Butanol concentrations, the range where it affects bubble formation and how sensitive bubble formation is to concentration changes, is vital. Seawater experiments at the SUSTAIN facility in Miami, Florida, were conducted in May 2017. Bubble measurements in the mentioned facility will reveal new insights of the comparability between Butanol conditions and seawater.
For extreme wind conditions with Butanol and enormous bubble densities, a precise bubble detection is not possible any more. A factor might be defined, which represents the reduction of the background intensity and thus determines a simple measure of bubble density.

Furthermore residence times, which can be determined by rise velocities, are interesting. Rise velocities can be obtained by evaluating consecutive images and bubble tracking of the existing bubble data from the Aeolotron.

A. Appendix

A.1. Measurement results of all campaigns

A.1.1. Aeolotron Heidelberg

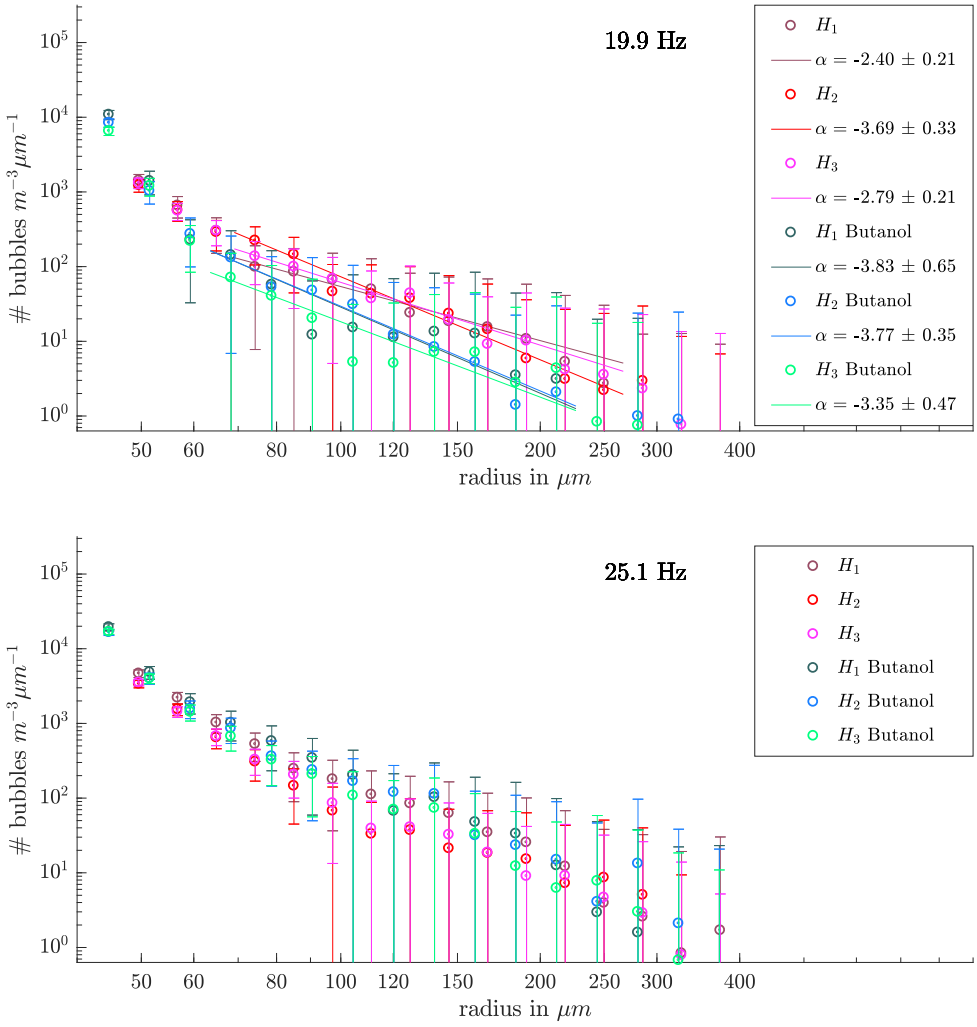

Figure A.1.: Bubble size distributions at H_1 to H_3 for wind speeds given in $f_{\text{ref}} = 19.9\,\text{Hz}$ and 25.1 Hz . Aeolotron, Heidelberg.

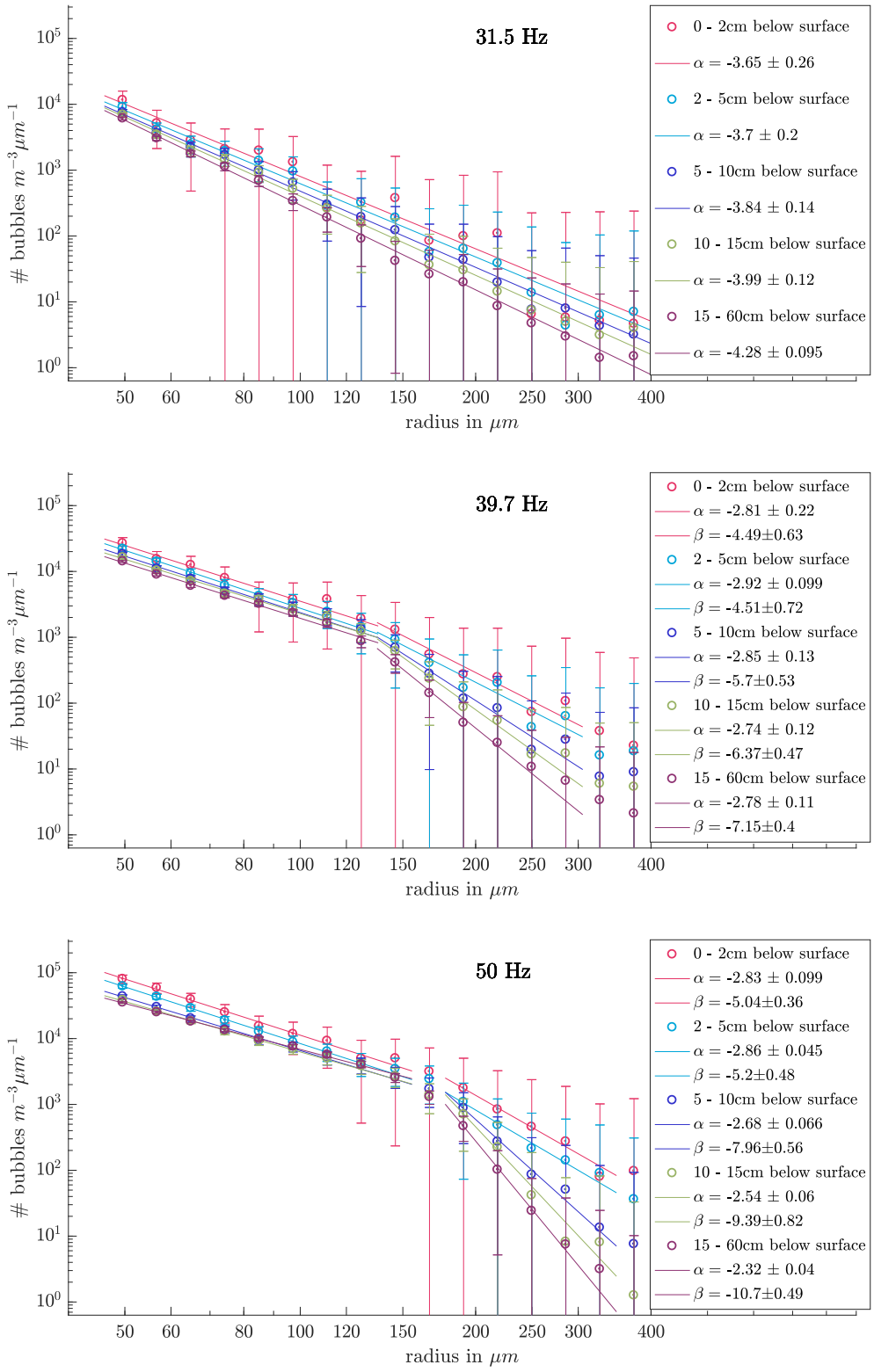

Figure A.2.: Bubble density in various absolute distances to water surface with VE water. Aeolotron, Heidelberg.

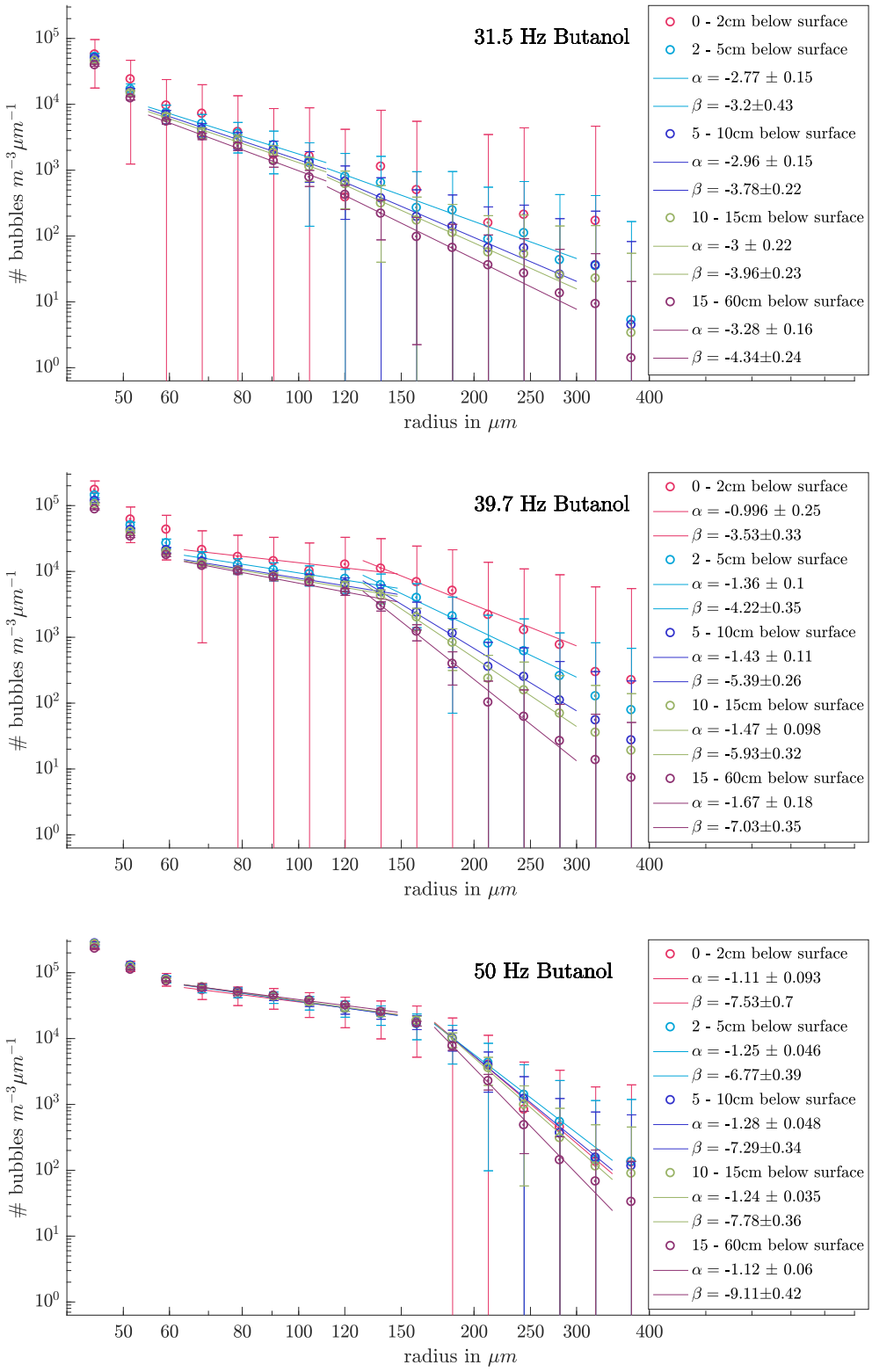

Figure A.3.: Bubble density in various absolute distances to water surface with Butanol. Triggering at the upper heights failed for the condition at 50 Hz, explaining that no clear height dependence is displayed. Aeolotron, Heidelberg.

A.1.2. Luminy - Marseille

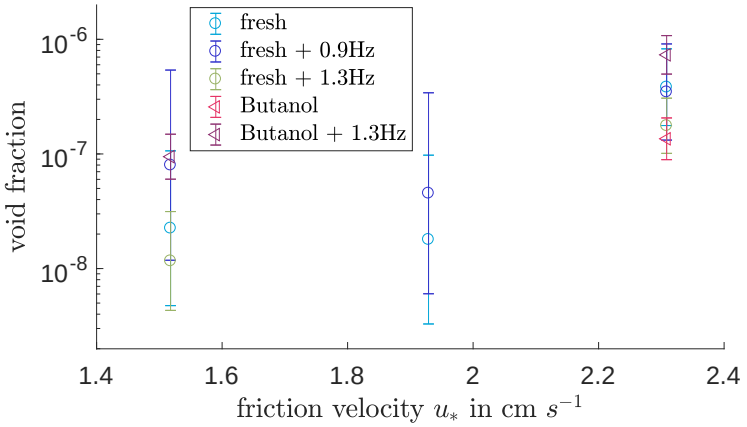

Figure A.4.: Void fraction dependent on u_*. Luminy, Marseille.

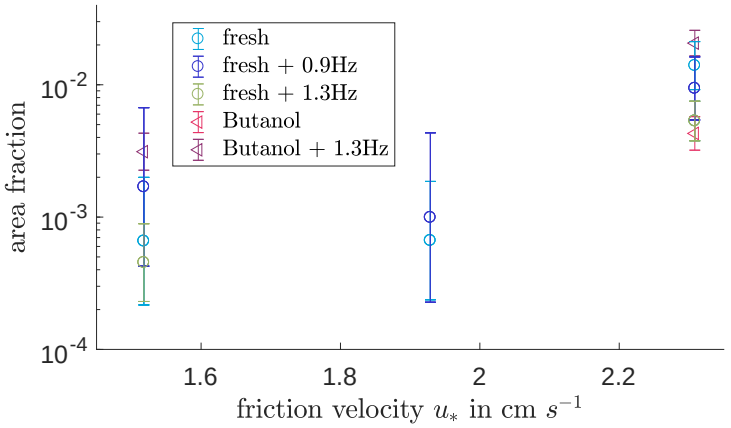

Figure A.5.: Area fraction dependent on u_*. Luminy, Marseille.

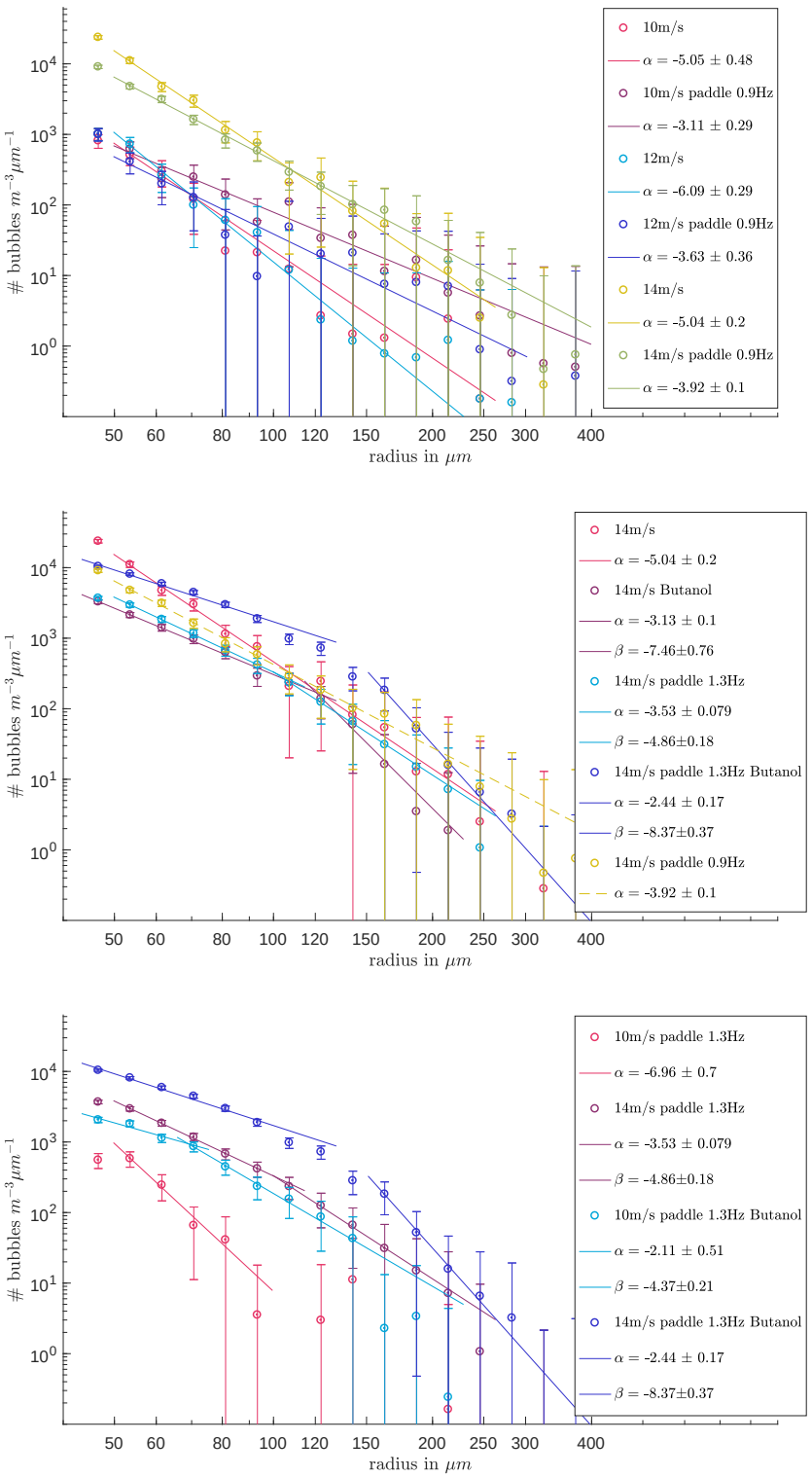

Figure A.6.: Bubble size distributions at various conditions. The activation of the mechanical paddle is indicated in the legend, paddle frequencies are given in Hz. Luminy, Marseille

A.1.3. Kyoto

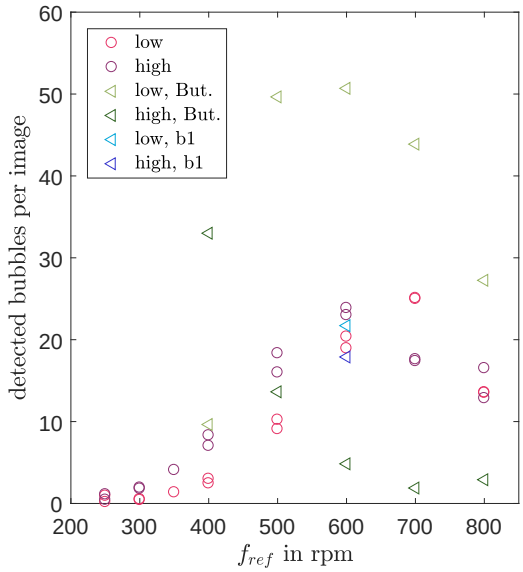

Figure A.7.: Number of detected bubbles per picture averaged over the entire condition. Kyoto.

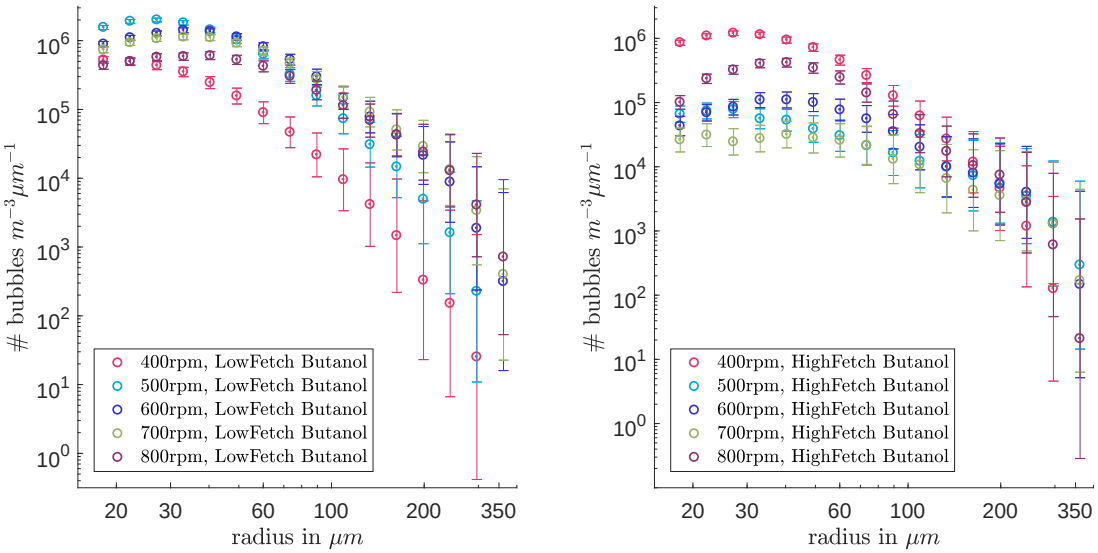

Figure A.8.: Bubble size distributions for Butanol conditions in the wind wave channel in Kyoto at low and high fetch.

A.2. Butanol concentrations

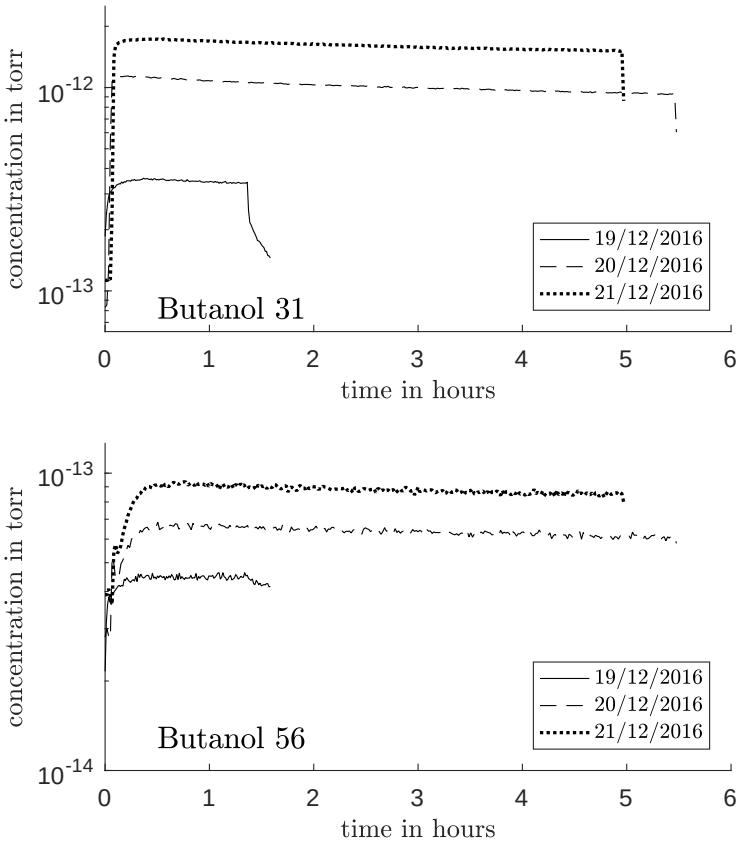

Figure A.9.: Measured partial pressure of Butanol over time for the measuring days 19.-21.12.2016 in Heidelberg. Partial pressure can be seen as a measure of concentration. Measurements are performed by a mass spectrometer which splits the Butanol molecule into a 31 u molecule and a 56 u molecule, monitored above.

A.3. Characteristics of optical filter

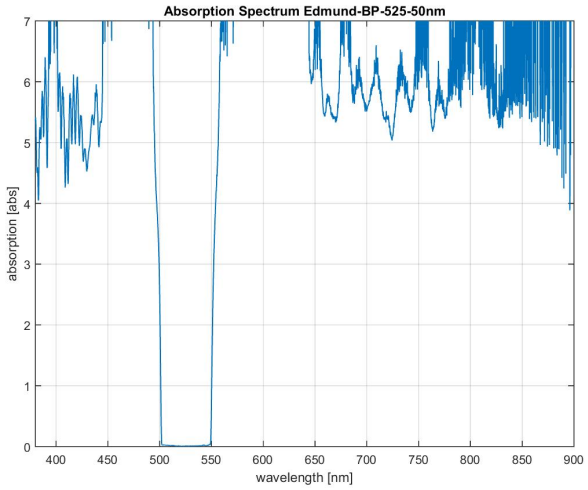

Figure A.10.: Green bandpass filter. Edmund optics. $525 \pm 25\,\mathrm{nm}$. Used for measurements in Marseille.

Bibliography

[1] G. Balschbach. Verschiedene Verfahren zur Visualisierung und Größenbestimmung von Gasblasen in Wasser. Diplomarbeit, Institut für Umweltphysik, Fakultät für Physik und Astronomie, Univ. Heidelberg, 1994.

[2] M. Bopp. Luft- und wasserseitige strömungsverhältnisse im ringförmigen heidelberger wind-wellen-kanal (aeolotron). Masterarbeit, Institut für Umweltphysik, Universität Heidelberg, Germany, 2014.

[3] M. Bopp. *Dissertation in preparation.* PhD thesis, Institut für Umweltphysik, Universität Heidelberg, Germany, 2017.

[4] N. D. Breitz and H. Medwin. Instrumentation for in situ acoustical measurements of bubble spectra under breaking waves. *The Journal of the Acoustical Society of America*, 86(2):739–743, 1989.

[5] G. Caulliez. Dissipation regimes for short wind waves. 118(2):672–684, 2013.

[6] M. Coantic and P. Bonmarin. The air-sea interaction simulation facility at the Institut de Mecanique Statistique de la Turbulence. *Atmospheric Technology*, 7:72–79, 1975.

[7] V. S. J. Craig. Bubble coalescence and specific-ion effects. *Current Opinion in Colloid & Interface Science*, 9(1-2):178 – 184, 2004.

[8] G. B. Deane and M. D. Stokes. Scale dependence of bubble creation mechanisms in breaking waves. *Nature*, 418:839–844, 2002.

[9] W. Gander, G. H. Golub, and R. Strebel. Least-squares fitting of circles and ellipses. *BIT Numerical Mathematics*, 34(4):558–578, Dec. 1994.

[10] P. Geißler. Depth-from-focus Bildanalyseverfahren zur Messung der Konzentration und Größe von Blasen und Mikroorganismen. Diplomarbeit, Institut für Umweltphysik, Fakultät für Physik und Astronomie, Univ. Heidelberg, 1993.

[11] P. Geißler. *Depth-from-Focus zur Messung der Größenverteilung durch Wellenbrechen erzeugter Blasenpopulationen.* Dissertation, IWR, Fakultät für Physik und Astronomie, Univ. Heidelberg, 1998.

[12] D. T. Ho, R. Wanninkhof, P. Schlosser, D. S. Ullman, D. Hebert, and K. F. Sullivan. Toward a universal relationship between wind speed and gas exchange: Gas transfer velocities measured with 3he/sf6 during the southern ocean gas exchange experiment. 116:C00F04, 2011.

[13] G. C. Holst and T. S. Lomheim. *CMOS/CCD Sensors and Camera Systems.* SPIE Press, Bellingham, Washington, USA, 2007.

[14] M. Honkanen, P. Saarenrinne, T. Stoor, and J. Niinimaki. Recognition of highly overlapping ellipse-like bubble images. 16(9):1760–1770, September 2005.

[15] B. Jähne. Air-sea gas exchange. In J. H. Steele, K. K. Turekian, and S. A. Thorpe, editors, *Encyclopedia Ocean Sciences*, pages 147–156. Elsevier, 2009. invited.

[16] B. Jähne. *Digitale Bildverarbeitung und Bildgewinnung.* Springer, 7. edition, 2012.

[17] B. Jähne, T. Wais, and M. Barabas. A new optical bubble measuring device; a simple model for bubble contribution to gas exchange. In W. Brutsaert and G. H. Jirka, editors, *Gas transfer at water surfaces*, pages 237–246, Hingham, MA, 1984. Reidel.

[18] K. E. Krall. *Laboratory Investigations of Air-Sea Gas Transfer under a Wide Range of Water Surface Conditions.* Dissertation, Institut für Umweltphysik, Fakultät für Physik und Astronomie, Univ. Heidelberg, 2013.

[19] K. E. Krall and B. Jähne. First laboratory study of air-sea gas exchange at hurricane wind speeds. 10:257–265, 2014.

[20] J. Kunz. *Active Thermography as a Tool for the Estimation of Air-Water Transfer Velocities.* PhD thesis, 2017.

[21] H. Medwin and N. D. Breitz. Ambient and transient bubble spectral densities in quiescent seas and under spilling breakers. *Journal of Geophysical Research: Oceans*, 94(C9):12751–12759, 1989.

[22] W. Mischler. Entwicklung eines Experiments zur Messung von Blasendichten und blaseninduziertem Gasaustausch. Diplomarbeit, Institut für Umweltphysik, Fakultät für Physik und Astronomie, Univ. Heidelberg, 2010.

[23] W. Mischler. *Systematic Measurements of Bubble Induced Gas Exchange for Trace Gases with Low Solubilities.* Dissertation, Institut für Umweltphysik, Fakultät für Physik und Astronomie, Univ. Heidelberg, 2014.

[24] P. D. Nightingale, G. Malin, C. S. Law, A. J. Watson, P. S. Liss, M. I. Liddicoat, J. Boutin, and R. C. Upstill-Goddard. In situ evaluation of air-sea gas exchange parametrization using novel conservation and volatile tracers. 14:373–387, 2000.

[25] K. Richter. Technische daten des aeolotron nach dem umbau 2007/2008. Technical report, AG Bildverarbeitung Interdisziplinäres Zentrum für Wissenschaftliches Rechnen und Institut für Umweltphysik, Universität Heidelberg, 2009.

[26] R. Rocholz and B. Jähne. Spatio-temporal measurements of short wind water waves. In *EGU General Assembly 2010, Symposium AS2.2*, pages EGU2010–5509, 2010.

[27] K. Schwarz. *Spatio-temporal measurements of water-wave height and slope using laser-induced fluorescence and splines.* Heidelberg, 2016.

[28] M.-Y. Su and J. Cartmill. Effects of salinity on breaking wave generated void fraction and bubble size spectra. In B. Jähne and E. Monahan, editors, *Air-Water Gas Transfer, Selected Papers, 3rd Intern. Symp. on Air-Water Gas Transfer*, pages 305–311, Hanau, 1995. AEON.

[29] N. Takagaki, S. Komori, N. Suzuki, K. Iwano, T. Kuramoto, S. Shimada, R. Kurose, and K. Takahashi. Strong correlation between the drag coefficient and the shape of the wind sea spectrum over a broad range of wind speeds. 39, 2012.

[30] D. K. Woolf and E. C. Monahan. Bubbles and the air-sea transfer velocity of gases. *Atmosphere-Ocean*, 31:517–540, 1993.

[31] D. K. Woolf and S. A. Thorpe. Bubbles and the air-sea exchange of gases in near-saturation conditions. 49(3):435–466, 1991.